RES | THE SCHOOL for RENEWABLE ENERGY SCIENCE

NUMERICAL MODELING OF THE NUCLEATION CONDITIONS OF PETAL-CENTERLINE FRACTURES BELOW A BOREHOLE FLOOR, A SENSITIVITY STUDY AND APPLICATION TO THE COSO GEOTHERMAL FIELD

Tryana Veronica Garza Cruz

UNIVERSITY OF ICELAND

University of Akureyri

NUMERICAL MODELING OF THE NUCLEATION CONDITIONS OF PETAL-CENTERLINE FRACTURES BELOW A BOREHOLE FLOOR, A SENSITIVITY STUDY AND APPLICATION TO THE COSO GEOTHERMAL FIELD

Tryana Veronica Garza Cruz

A 30 ECTS credit units Master´s thesis

Supervisor

Dr. Nicholas Davatzes

A Master´s thesis done at

RES | The School for Renewable Energy Science

in affiliation with

University of Iceland &

University of Akureyri

Akureyri, January 2010

Numerical modeling of the nucleation conditions of petal-centerline fractures below a borehole floor, a sensitivity study and application to the Coso Geothermal Field

A 30 ECTS credit units Master´s thesis

RES | The School for Renewable Energy Science

Solborg at Nordurslod

IS600 Akureyri, Iceland

Telephone + 354 464 0100

www.res.is

Printed in (2010)

at Stell Printing in Akureyri, Iceland

ABSTRACT

A numerical model using Poly3D© has been developed to simulate the stress concentration below the floor of a borehole and investigate the conditions in which petal-centerline fractures induced by this stress perturbation could nucleate. The geometry, stress state, and traction boundary conditions on the borehole surface are taken from direct measurements in the 58A-10 borehole of the Coso Geothermal Field, CA in which the occurrence of petal-centerline fractures are confirmed by image logs. These results have been validated against the simpler 2D analytical Kirsch solution, which was also used to balance the computational intensity against a sufficiently accurate characterization of local stress states close to the modeled borehole surface. A sensitivity analysis revealed that material properties such as Poisson's ratio has little impact on tension, whereas outward directed traction boundary conditions on the borehole surface including weight on bit and excess drilling mud pressure suppress tensile stress below the borehole. The potential for tension below the borehole floor was quantified for all frictionally permissible stress states in the Earth's brittle crust revealing that petal-centerline fractures in vertical boreholes are favored in normal faulting environments. However, this behavior is highly sensitive to borehole deviation and deviation direction such that increased deviation towards S_{Hmax} increases tension by more than an order of magnitude over the vertical borehole in the stress state at the Coso Geothermal Field. These results demonstrate that the occurrence of petal-centerline fractures in cores or image logs of borehole walls constrain the sate of stress in the shallow Crust.

ACKNOWLEDGEMENTS

I am deeply thankful to my supervisor Dr. Nicholas Davatzes whose guidance, support and endless patience made this thesis possible. I appreciate his vast knowledge and the opportunity to work with him in his Laboratory at Temple University in Philadelphia, USA.

I would like to thank the access to Poly3D and aid in model development provided by Frantz Maerten, Dr. Laurent Maerten and Jean Pierre Joonnekindt of IGEOSS in Montpellier, France.

I am profoundly grateful for the financial and academic support from The School for Renewable Energy Science, especially to Rector Dr. Björn Gunnarsson, Academic Coordinators Dr. Axel Bjornsson and Dr. Hrefna Kristmannsdottir, and Office Managers Sigrún Lóa Kristjánsdóttir and Zane Brikovska.

I would also like to express my gratitude to my fellow RES students for their support and help, as well as to Masami Nakagawa for his advice.

I am grateful to my family, Francis and Alberto for their love and endless support, and Diego for his encouragement, love and patience.

TABLE OF CONTENTS

LIST OF FIGURES

LIST OF TABLES

1 INTRODUCTION

Geothermal Energy is a clean and reliable source of energy that can help reduce pollution while providing energy security. According to a recent assessment led by MIT, Enhanced Geothermal Systems could supply in the USA alone at least 100 GWe of cost-competitive electricity generation capacity in the next 50 years with a reasonable investment in research and development (Tester, et al., 2006). Several geothermal systems related processes such as drilling, induced seismicity and the development of enhanced geothermal systems are strongly related to the prediction of fracture behavior underground.

Enhanced Geothermal Systems are typically developed in locations where heat is abundantly available, but the permeability or saturation necessary to extract that heat are insufficient. In this circumstance permeability must be artificially increased and concurrently water injection pressure support provided. The most common method to increase permeability is via hydraulic fracturing. This creates a network of fractures that could allow water to travel from an injection to a production well while extracting heat from the neighboring hot rock. Predicting the pressures required to initiate fracture, and resulting orientation and distribution of fractures created during hydraulic fracturing that define the new enhanced (or engineered) reservoir is critical to successful stimulation and connection between wells. The orientation of fractures activated by increased fluid pressure is dictated by the stress state in the vicinity of the well. Similarly, the magnitudes of the stress components will determine the pressures in which reactivation of natural fractures in shear or formation of new tensile fractures will occur. Therefore, the identification and quantification of the underground principal stress directions and their relative magnitudes is critical to both hydraulic stimulation of hot dry rock and the location and orientation of wells that can access the stimulated volume. More generally, the same remote principal stresses also interacting with hydraulically induced fractures govern earthquakes and plate tectonics.

Image logs are commonly used to characterize wellbores, the surface geometry of the borehole wall, and natural fractures that intersect the borehole. In addition to the natural population of fractures in geologic formations, image logs reveal deformation of the borehole induced by the in situ rock stresses resolved on the borehole walls. These remote principle stresses are amplified by the presence of the borehole. In the past, structures resulting from these stresses include breakouts, which form due to compressive failure of the borehole wall where compressive hoop stresses are enhanced (Zoback, Moos, Mastin, & Anderson, 1985), and tensile fractures, which form in response to tensile hoop stresses induced at the borehole wall (Zoback M. , et al., 2003). Comparisons of theoretical models with experiment (Haimson & Fairhurst, 1967; Haimson & Herrick, 1989) reveal that these structures reliably indicate the directions and constrain the magnitudes of the remote principal stresses. Thus the identification of these structures in image logs is routinely used to interpret the orientations of remote principal stresses, and less frequently to model their magnitudes. Because of the symmetry of the locally perturbed stress state around the borehole, both borehole breakouts and tensile fractures occur in pairs 180° apart. In vertical boreholes, and Andersonian stress states (Anderson, 1951; Jaeger, Cook, & Zimmerman, 2007) in which one principal stress is vertical, breakouts occur parallel to the angle of the minimum horizontal principal stress (S_{hmin}) and tensile fractures along the angle of the maximum horizontal principal stress (S_{Hmax}) and are thus offset by 90°. Both breakouts and tensile fractures require a significant difference between the principal stresses acting in the plane orthogonal to the borehole axis to produce a large enough stress perturbation to overcome large compressive rock strength in the case of breakouts and to overcome the otherwise compressive stress environment at depth in the case of tensile fractures. Other factors such as the *in situ* fluid pressure of water in the pores of the surrounding rock formations, the fluid pressure in the borehole resulting from drilling mud pressure, and cooling of the borehole during drilling also contribute to local changes in stress in the vicinity of the borehole.

1.1 Petal-Centerline Fractures

A third, drilling induced structure, called petal centerline fractures, was first recognized in core recovered from boreholes (Figure 1a) (Kulander, Dean, & Ward, 1990). In coring operations, petal centerline fractures have been hypothesized to form ahead of the drill bit due to a complex concentration of stresses which are maximized by the high degree of curvature along the inner kerf corner produced by coring bits (Li & Schmitt, 1997). Subsequently, similar geometries have been reported in image logs of the borehole wall (Figure 1b) (Davatzes & Hickman, Stress And Faulting in the Coso Geothermal Field: Update and Recent Results from the East Flank and Coso Wash, 2006; Rose, et al., 2006). Much like tensile fractures, the hypothesis is that these fractures form in response to tension induced by the borehole, but in this case below the bottom of the wellbore. According to this hypothesis, the distribution of stress concentrations at the bottom of a wellbore dictates the formation and geometry (orientation) of petal-centerline fractures. Whereas the stress concentration around the borehole wall far removed from the base or top of the borehole approximates a plane strain condition that is easily modeled via the analytical Kirsch solution to the elastic stress boundary value problem, there is no similar solution for the stress concentration at the borehole floor. Thus, petal centerline fractures are far less understood, and currently often go un-recognized or unused.

In order for petal-centerline fractures to be captured in core, they must propagate below the borehole floor. Plumose structure indicative of Mode I fracture further indicates that they initiate below the borehole floor but extend beyond the footprint of the borehole, thus enabling them to be captured in image logs (Kulander, Dean, & Ward, 1990). As Mode I fractures the petals propagate perpendicular to the local least compressive principal stress. The attitude and magnitude of the local stress is highly sensitive to proximity to the borehole where it must rotate into parallelism with the free surface of the borehole floor (Figure 2a). In vertical wells aligned with the vertical principle stress, these fractures must thus curve to become parallel with the borehole axis and are then called a centerline fracture (example in Figure 1b, cartoon of progressive propagation in Figure 2b)(Rose, et al., 2006). In core and in image logs from vertical wells, the orientation of these drilling-induced fractures appear to systematically correlate with the remote principal stress orientations as verified by comparison to the orientation of induced tensile fractures and breakouts in image logs from a limited number of examples from vertical boreholes (Rose, et al., 2006; Li & Schmitt, 1997). Previous work has preliminarily explored the sensitivity of petal centerline fracture to formation under various stress boundary conditions on a flat-bottom borehole corresponding to the Coso Geothermal Field (Rose, et al., 2006) and to elastic constants, coring curve geometry, and some remote stress conditions in vertical boreholes (Li and Schmidt, 1997).

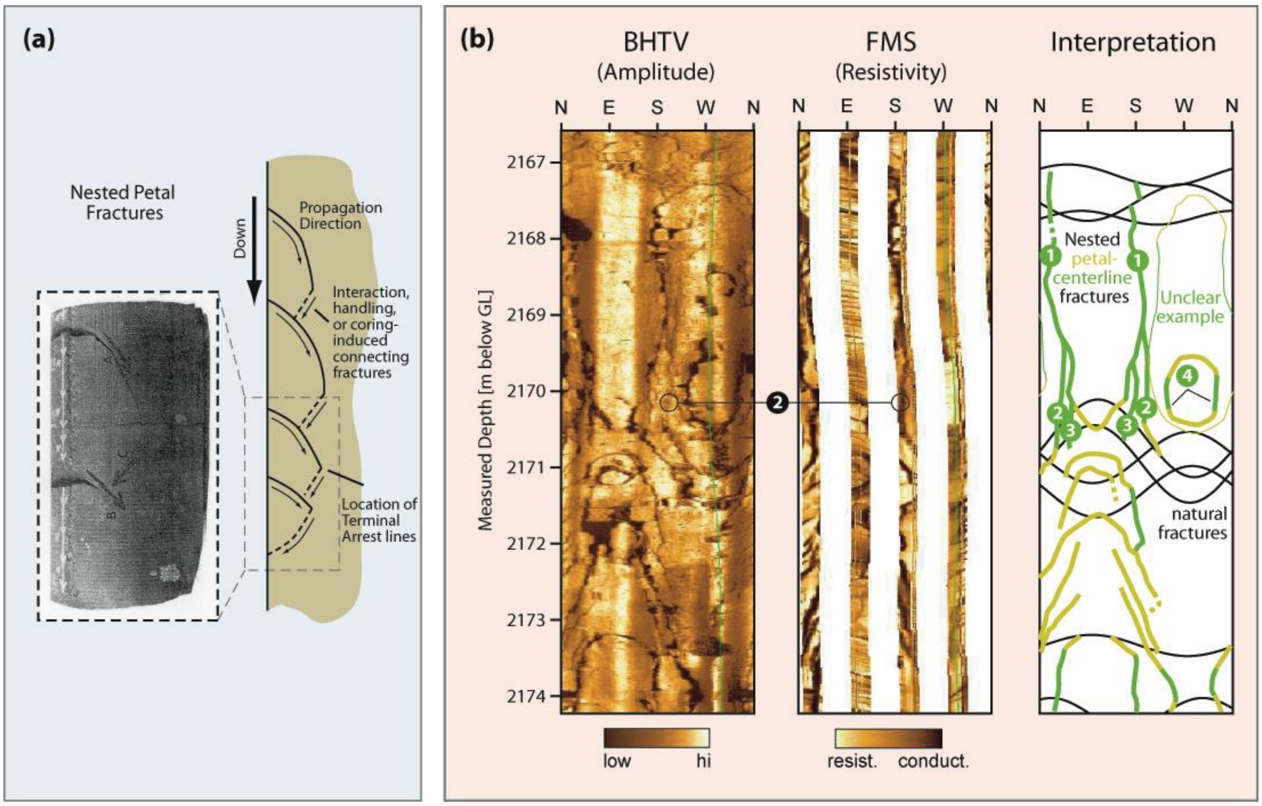

Figure 1. Nested petal centerline fractures (a) in core from an oil and gas well (modified from Kulander et al., 1990), and from a geothermal well (b) in BHTV and FMS data; the sketch illustrates the nesting and sequential growth of petal (light green) and centerline (dark green) fractures similar to the core example (from Davatzes and Hickman, 2006, in Rose, et al., 2006).

As Mode I fractures, petal centerline fracture nucleation depends on the generation of tension sufficient to overcome the tensile strength of the rocks the borehole is drilled through. The theoretical strength of a material is given by the force that must be applied to extend the inter-atomic separation distance until an energy barrier is overcome and a crack can propagate through the material (Sanford, 2003). Theoretical strength values are usually orders of magnitude higher than the actual strength of a material. This discrepancy is mainly attributed to the presence of flaws and small fractures. These flaws act as stress concentrators at the crack tip, leading to local stresses that exceed the strength of the material and cause crack propagation even at small applied loads (Sanford, 2003). This stress concentration is geometry dependent, but the concept has been generalized into a characteristic material property known as the stress intensity factor. When the stress intensity factor reaches a critical value known as the fracture toughness the material will fail. When a crack is oriented parallel to the maximum principal compressive stress a tensile stress is generated and amplified at the crack tip. If the stress intensity factor reaches the fracture toughness of the material, the crack will extend and propagate in the plane orthogonal to the maximum principal stress in opening mode (Mode 1). Therefore, the distribution of the principal stresses and inherent flaws controls the initiation and direction in which a fracture propagates. In most rocks, this implies that even small amounts of tension are capable of initiating Mode I fracture. Thus in the case of petal centerline fractures, tension should be sufficient to cause their formation, especially considering the inherent roughness of the borehole floor which will locally amplify even small amounts of tension and thus promote Mode I fracture initiation.

A better insight into the conditions promoting the tensile stress to nucleate petal-centerline fractures can be obtained by numerical modeling of the interaction between the remote principal stresses, local borehole conditions, and borehole geometry (particularly inclination of the borehole). These numerical tests are critical to determining: (1) under what stress conditions tension is developed, (2) whether petal centerline fractures are reliable indicators of remote principal stress directions, (3) how their geometry changes where the well is inclined to the principal stresses, (4) whether they can be used to model stress magnitudes. This study focuses on the local stress conditions resulting from concentration of stress at the bottom of the borehole and draws implications for their use in estimating the remote stress magnitudes and directions.

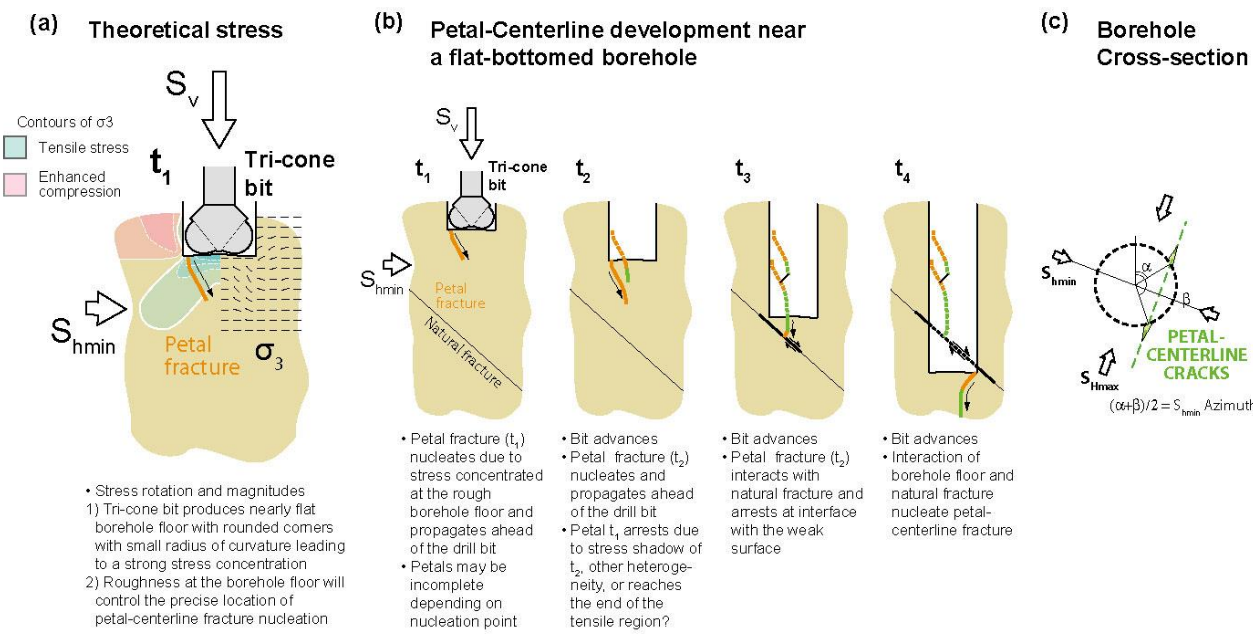

Figure 2. Conceptual Model of petal centerline fracture nucleation and propagation (from Davatzes and Hickman, 2006, in Rose, et al., 2006)

2 NUMERICAL METHODS: POLY3D AND OVERVIEW OF ANALYSIS APPROACH

2.1 Poly3D

The working hypothesis is that contributions from the remote principal stresses, tractions on the borehole walls and floor, and the borehole geometry can produce tension sufficient to induce tensile fracture necessary to explain petal-centerline formation. This elastic stress perturbation associated with the bottom of a well is simulated using Poly3D (Thomas, 1993), a numerical boundary element code that solves the linear elastic, homogeneous, isotropic boundary value problem. Poly3D uses triangular elements capable of simulating complex geometric shapes such as curved borehole surfaces based on the boundary element method of Crouch and Starfield, 1983. These elements act as surfaces of displacement discontinuity and are used to calculate the quasi-static displacements, stresses and strains induced in a whole- or half- space (Thomas, 1993; The Stanford Rock Fracture Project, 2002). Poly3D is a C++ language program available in two formats: (1) a iterative solver implementing inequality boundary conditions on the elements and accessible through a commercial GUI interface from IGEOSS; (2) a direct solver compiled on UNIX that can be slaved to Matlab routines and run in batches. Initial exploration of the behavior of the stress concentration under different boundary conditions was explored via the GUI. Subsequently, larger batch files that explored the impact of these boundary conditions of a range of reasonable values were explored via Matlab.

Modeling complex geometries with rectangular elements leads to the introduction of gaps and overlaps with associated stress concentrations that are usually unrealistic. By introducing planar triangular elements, Poly3D avoids this problem and closely approximates curvi-planar surfaces. Such surfaces can be made smoother by decreasing the size of the elements forming a surface. A distinct advantage of boundary element methods is that they only require meshing of surfaces, and thus allow modeling of complex geometries with a lower computational load than required by Finite Element Methods, which require meshing of an entire volume. This was a distinct advantage for exploring the large range of boundary conditions that could impact development of tension at the borehole floor.

The program includes the application of localized tractions and/or displacement boundary conditions to the triangular elements as well as homogeneous remote stresses or strains. When all the elements in a body have displacements prescribed as boundary conditions, the displacement at any point is determined by summing the contribution of all elements within the elastic body. On the other hand, when the elements have been prescribed with tractions as boundary conditions, an additional step has to be computed in which the displacement fields produced by these tractions are calculated, then superposed as above; the final stress field is inverted from these displacements. The remote stress assigned to a model is applied into each triangular element as tractions resolved from this remote stress. If a remote strain is applied instead, Hooke's Law is used to calculate the far field stress first and then applied as above (Maerten, Maerten, Pollard, & Lagalay, 2009). Poly3D superposes the stress components caused by displacement discontinuities across boundary elements with those components induced by the far field stresses to calculate the total stress at specified observation points. Therefore, as soon as all the displacement discontinuities are known, displacement, strain, and stress can be computed at any observation point within the elastic volume (Soliva, Maerten, Petit, & Auzias).

2.2 Analysis Approach

Since petal-centerline fractures have been identified in the Coso Geothermal Field borehole 58A-10(Davatzes & Hickman, in press) where the stress field is also well-constrained, models used in this study reflect this borehole's geometry. A flat-bottomed cylindrical surface of 0.15875 m in diameter was created to study the concentration of stresses below the borehole floor. The well extended from the floor 7.5 well diameters up the well axis to isolate the bottom-hole stresses from effects of the upper well termination. To reduce the computational intensity of the simulation, the well was divided into four segments; a finer mesh was created for the bottom segment and the floor, since that's the region of interest for petal-centerline formation, and coarsened up in the subsequent segments as it gets farther away from the floor. A set of observation points was also implemented covering a volume of around 64 cubic radiuses to survey the concentration of stresses near the bottom of the well. The modeled well and the volume of observation points used are shown in Figure 3.

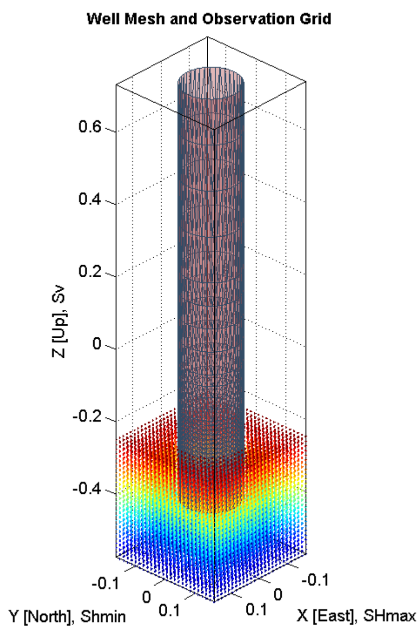

Figure 3. Modeled well and observation volume. The well is divided into 4 main segments that coarsen up as they get farther away from the borehole floor. The observation points are colored as a function of their position.

A mesh analysis against the Kirsch solution was first performed to determine the density of the mesh, ensuring the capture of a significant portion of the stress concentration while staying away from the non-physical influence of the dislocations (section 3.1). A model of well 58A-

10 was constructed with the derived parameters, and a sensitivity study on the impact boundary conditions have on the concentration of stresses in the vicinity of the borehole bottom was performed (section 3.2). This allowed us to evaluate the effect the individual boundary conditions had over the generation of tension below the borehole floor. To study the effect different stress states would have on the maximum concentration of stresses on the walls and below the borehole floor, the modeled borehole was subjected to the 76 stress states, marked in Figure 20 (section 3.3). The sampled stress states are assumed to be representative of all permissible stress states in the Earth's crust. Using the stress state from Coso well 58A-10 a study on the effect of the deviation of the borehole along the principal directions was performed to analyze the geometrical distribution of stresses below the borehole (section 3.4.2). Finally, the well was modeled at 91 combinations of deviation and deviation directions, marked in Figure 31, to study the behavior of the maximum principal stress generated in the vicinity of the borehole floor as a function of well inclination (section 3.4.2). To do this the stress state was rotated relative the fixed modeled borehole using stress tensor transformation. As part of this study, the boundary conditions were varied to better visualize their impact on the maximum tensile stress generation.

3 RESULTS

3.1 Mesh Analysis compared to Kirsch's analytical solution

3.1.1 **Methods**

The 2D Kirsch solution reveals that the stress concentration is highest along the well surface, and implies similar behavior in the 3D case addressed by this work (Kirsch, 1898; see summary in Zoback, 2007). However, boundary elements do not allow direct observation of the stress state at the borehole wall because of the numerical approximation (and elastic strain gradients resulting in stress singularities) resulting from treating the elements discretizing the borehole surface as dislocations. Surveying into this region of singularity near element edges and corners would result in the calculation of non-physical stress magnitudes. To ensure the physical meaningfulness of the stresses computed using Poly3D, it was necessary to validate that the observation points in our numerical simulations are outside of the region contaminated by the stress singularities at element edges by validation against the analytical Kirsch solution. Aside from the dislocation cores at the corners of the triangular elements, the distance at which the non-physical stress approximation dominates is scaled to element size. As a consequence, the closer to the well surface stress is surveyed, the more computationally intense the model must become as element size is correspondingly reduced. Thus, it was necessary to balance the computation load resulting from smaller element size against a calculation of the stress concentration adequate to detect tension.

An iterative analysis was performed to establish the radial distance from the borehole surface at which the first point of the observation grid would be set and the actual dislocation element length. By performing this analysis both the borehole mesh density and the distance from the observation grid, were determined and implemented in all further simulations throughout this study. To quantify this relationship, a series of wells with different mesh density were constructed to reproduce the 2-D Kirsch solution. The Kirsch solution (Kirsch, 1898) in polar coordinates for the stress concentration outside a circular hole in an infinite elastic body with maximum horizontal far field principal stress S_{Hmax} acting in the θ = 0 direction and minimum horizontal far field principal stress S_{hmin} acting 90° from θ is:

$$\sigma_{rr} = \frac{(S_{Hmax} + S_{hmin} + 2P_p)}{2}\left[1 - \left(\frac{R}{r}\right)^2\right] + \frac{(S_{Hmax} - S_{hmin})}{2}\left[1 - 4\left(\frac{R}{r}\right)^2 + 3\left(\frac{R}{r}\right)^4\right]\cos 2\theta - dP\left(\frac{R}{r}\right)^2, \quad (1)$$

$$\sigma_{\theta\theta} = \frac{(S_{Hmax} + S_{hmin} + 2P_p)}{2}\left[1 + \left(\frac{R}{r}\right)^2\right] - \frac{(S_{Hmax} - S_{hmin})}{2}\left[1 + 3\left(\frac{R}{r}\right)^4\right]\cos 2\theta + dP\left(\frac{R}{r}\right)^2, \quad (2)$$

$$\sigma_{r\theta} = \frac{(S_{Hmax} - S_{hmin})}{2}\left[1 + 2\left(\frac{R}{r}\right)^2 - 3\left(\frac{R}{r}\right)^4\right]\sin 2\theta \quad (3)$$

where r is the distance from the center of the hole, R is the radius of the hole and dP is the difference between the drilling mud pressure and the formation pore pressure P_p. At the surface of the hole, where R=r, the hoop stress $\sigma_{\theta\theta}$ varies from a maximum value of $3\sigma'_{hmin} - \sigma'_{Hmax} + \Delta P$ when θ = 0, or π, to a minimum value of $3\sigma'_{Hmax} - \sigma'_{hmin} + \Delta P$ when θ = π/2 or 3π/2. Where σ'_{Hmax}=$S_{Hmax} + P_p$ is the maximum horizontal effective stress, and σ'_{hmin}=$S_{hmin} + P_p$ is the minimum horizontal effective stress. The difference between the maximum and minimum hoop stress is $4(\sigma'_{Hmax} - \sigma'_{hmin})$, which shows that the far field stress concentration around the borehole gets amplified by a factor of 4. This amplification is essentially applied to the mean stress in this solution, thus the potential for developing tension depends on both the differential and mean stresses.

The model meshes were constructed to simulate the central part of a well of 0.15875 m in diameter (6.25in) with ends to the mesh far removed from the observation grid centered on the borehole where the local stress tensor was calculated (see Figure 4). This distance is sufficient to reproduce a plane strain condition in the region of the observation grid and therefore to obtain results comparable to the analytical Kirsch solution for a circular cylinder in an infinite elastic body. This borehole diameter corresponds to borehole 58A-10 in Coso Geothermal Field of California, United States, where petal-centerline fractures are known to occur (Davatzes and Hickman, in press). This simpler case both validated the numerical approach and provided a method to calculate the percent difference between the analytical solution and numerically simulated stress tensor due to element size. It also provides insight into how much of the stress concentration is missed in these calculations where observations points are limited to a minimum distance from the mesh used to model the borehole walls, and in subsequent sections, its floor.

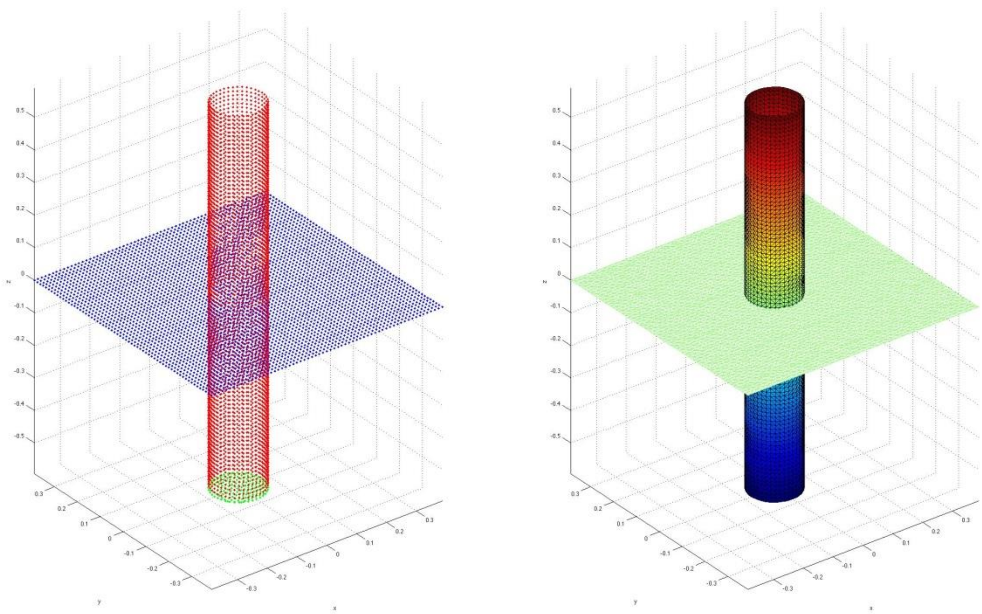

Figure 4. Model of the central part of a well formed by 40 circumferential elements, observation grid centered. Left: Well nodes and observation points where the stress concentrations are calculated. The borehole floor of similar mesh density is shown in green, but is neglected in the validation analysis. Right: Well mesh colored to show the distance along the borehole axis, and the observation grid as a surface orthogonal to the borehole axis.

3.1.2 **Results**

Five wells with different mesh density were modeled and subjected to a remote stress state of σ_1 = -10MPa and σ_2 =-20MPa (compression negative). The wells were circumferentially discretized into 10, 20, 30, 32 and 40 triangular elements. Table 1 summarizes the element dimensions in the circumferential direction and symbols used, note that the radius of the well is 0.0794 m.

Table 1. Dimensions used to model the well mesh and describing symbols.

Symbol	**Description**	**Element length [m]**	**Element length/ Radius**
Diamond	(2 π R)/10	0.0499	0.628
Square	(2 π R)/20	0.0249	0.314
Triangle	(2 π R)/30	0.0166	0.209
Dot	(2 π R)/32	0.0156	0.196
Circle	(2 π R)/40	0.0125	0.157

These five models (Table 1) were evaluated in Poly3D with stress boundary conditions σ_1 = -10 MPa acting in the x-direction and far field stress σ_2 =-20MPa acting in the y-direction. The resulting displacement and stress fields were calculated. The evolution of the local principal stresses σ_1 and σ_2 resolved on the observation points lying along the x and y-axis away from the borehole wall were plotted and compared to the Kirsch analytical solution (solid line) of an axially infinite cylindrical hole in an infinite elastic body subjected to the same far field stress. The stress components σ_{xx}, σ_{yy} and σ_{xy} were also contoured for comparison. Figure 5 shows the comparison of the five Poly3D models associated with different well discretization to the analytical Kirsch solution along the x-axis while Figure 6 shows them along the y-axis. At a distance of 0.12 m from the axis of the well, all Poly3D models converge with the analytical solution regardless of well mesh density. The percent difference between the analytical Kirsch solution and numerical simulations as a function of the distance along the x-axis (parallel to σ_1) in Figure 7, and as a function of the distance along the y-axis (parallel to σ_2) in Figure 8 reveal that the solutions diverge by less than 20% at approximately 0.09m from the borehole axis. This distance is approximately equal to 0.8 element lengths in the well discretized by 40 circumferential elements.

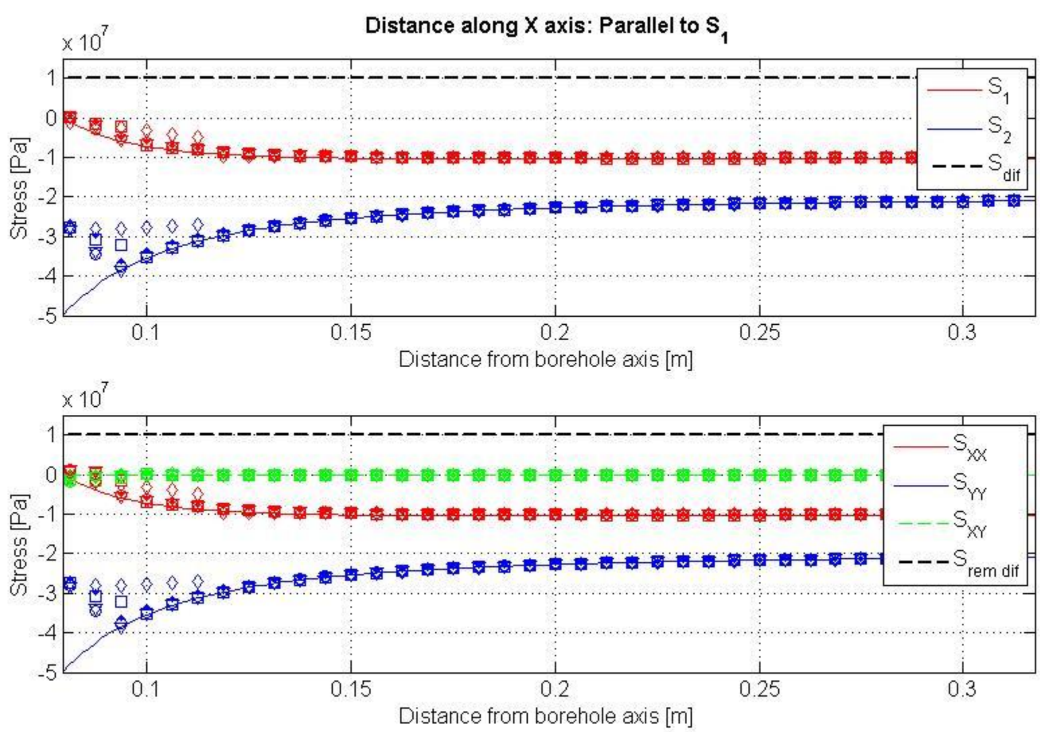

Figure 5. Evolution of the principal stresses (a), and stress components (b) along the x-axis and their comparison with the corresponding Kirsch solution.

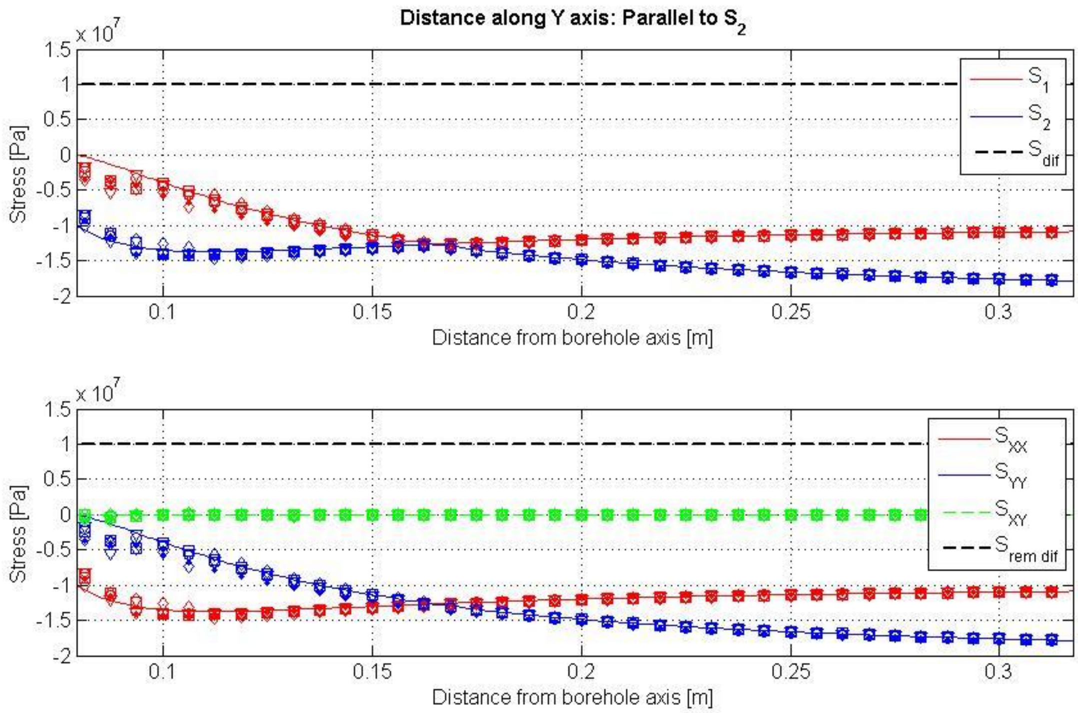

Figure 6. Evolution of the principal stresses (a), and stress components (b) along the y-axis and their comparison with the corresponding Kirsch solution.

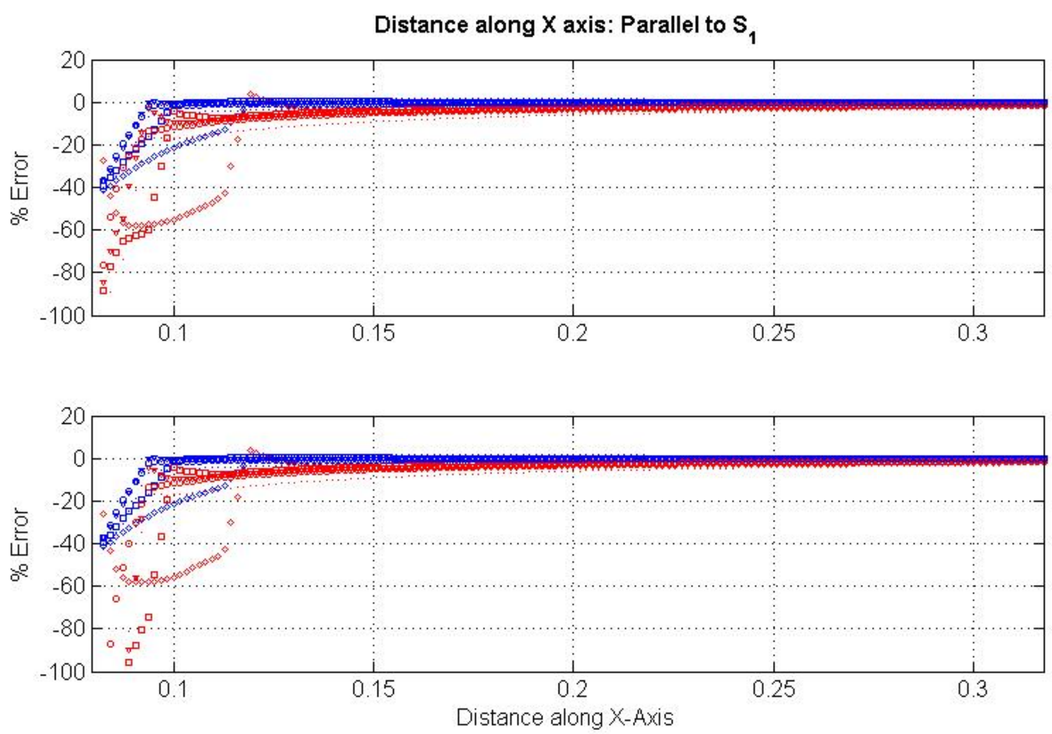

Figure 7. Percent error of the modeled cases with the Kirsch analytical solution along the x-axis.

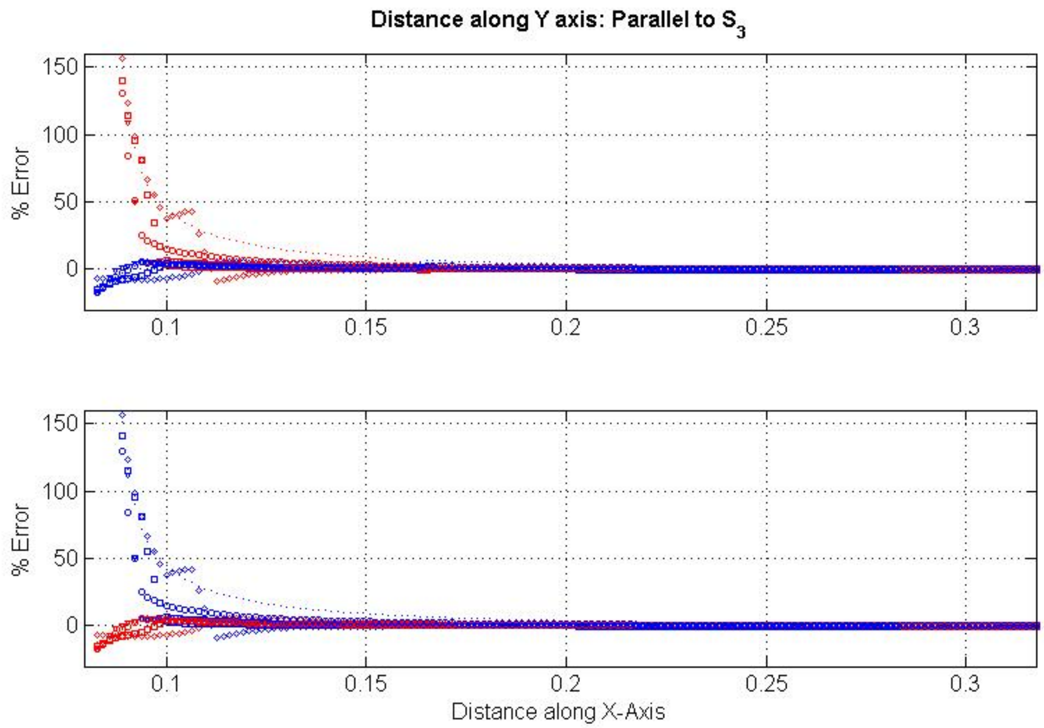

Figure 8. Percent error of the modeled cases with the Kirsch analytical solution along the y-axis.

The error analysis quantifies (1) the minimum surveying distance ensuring valid stress states and (2) the minimum optimum mesh density to ensure that the stress concentrations would have physical meaning while capturing a conservative estimate of the stress magnitude. Since σ_1 is the least compressive local principal stress, and thus first to reach tension, most of this study is focused on characterizing variation in its magnitude and direction. The top section of Figure 7 shows that the analytical value of σ_1 (red) was first and more steadily converged by the well discretized with 40 circumferential triangles (circles). An error of -20% was reached by such model at approximately one element length distance from the well (0.092 m from the well axis). The top portion of Figure 8 shows a similar behavior and gives an error of around 20% at the same distance from the well. Thus the 40 circumferential element well is a sufficient mesh density and the observation grid is required to exceed a distance of one element length from the borehole surface. Since the magnitude of stress components exponentially decays with increasing distance from the borehole to the remote stress magnitudes, stress magnitudes one element length from the well surfaces slightly underestimate the concentration of stresses at the surface of the borehole. Therefore estimates for the onset of formation of tensile and petal-centerline fractures will be very conservative. As a consequence of this analysis, the mesh density of the bottom section and floor of the modeled Coso well 58A-10 was set to 40 circumferential elements, with an observation grid standing one element distance away. Such model is used in all following sections, and as proved above, it provides a conservative estimate on the maximum tensile stresses resolved on the borehole floor vicinity. The stresses presented in the results below were surveyed at a distance of at least one mesh element length away from the modeled well surface, as suggested by this analysis.

3.2 Impact of Boundary Conditions on the stress concentration near the borehole floor.

During drilling many factors contribute to the local perturbation of stress at the borehole floor. The synergistic effect of boundary conditions such as far-field stresses, drilling mud pressure, pore pressure and applied weight on bit (WOB) applied to a specific geometry may be difficult to visualize and predictions of the stress field at the bottom of the borehole become less obvious and intuitive. In an effort to better understand the specific contributions of the boundary conditions on a flat-bottomed borehole, different simulations focusing on each of these contributions individually at a time were run.

The vertical flat-bottomed well developed in the previous section was used to evaluate the contribution of each of the boundary conditions present during drilling. A total of 6 simulations were run. Table 2 summarizes the conditions studied. To facilitate comparison between cases, the most tensile local principal stress, σ_1, is shown in a planar grid of observation points parallel to the well axis and aligned at its center for each model. Where informative, a second observation grid perpendicular to the first is also shown. To facilitate comparison, the first three boundary conditions studied (WOB, Drilling Mud Pressure and Formation Pore Pressure) were plotted using the same $\sigma_1$color contour scale, since the magnitudes of the concentrated stress are similar. The scale extends from a compressive stress of -0.38 MPa (blue) to a tensile stress of 0.89 MPa (red). On the right side of each figure, the tickmarks (or disks) indicate the simulated orientation of opening mode failure planes orthogonal to σ_1; in each case the symbol size is scaled to the magnitude of σ_1.

Table 2. Boundary conditions used in the study of the individual contributions of drilling parameters.

Boundary condition	**Description**	**Magnitude [MPa]**	**Color contour scale [MPa]**
Weight on bit (*WOB*)	Applied as a normal traction pointing outwards the well floor	1	-0.38 to 0.89
Drilling Mud Pressure	Applied as a normal traction pointing outwards of the well walls and floor	1	-0.38 to 0.89
Formation Pore Pressure	Applied as a normal traction pointing inwards of the well walls and floor	1	-0.38 to 0.89
Uniform Remote Stress	Compressive uniform remote stresses	S_v = 1 S_{Hmax} = 1 S_{hmin} = 1	-1 to -0.125
Vertical Plane Remote Stress	Compressive vertical and maximum horizontal remote stress	S_v = 1 S_{Hmax} = 1 S_{hmin} = 0	-0.4 to 0.42

Horizontal Plane Remote Stress	Compressive maximum and minimum horizontal remote stress	$S_v = 0$ $S_{Hmax} = 1$ $S_{hmin} = 1$	-0.29 to 0.17

- Weight on Bit

A series of normal tractions were applied at the centroid of each triangular element forming the floor surface of the modeled borehole to simulate the application of weight on bit while drilling a borehole. The tractions were assigned a downward direction and only applied at the borehole floor with a magnitude of 1 MPa. As a result, tensile stress was resolved in the three local principal stress directions on the lower section of the wall near the bottom with the maximum principal local stress being in the S_{rz} direction (using a polar coordinate reference frame), as well as on the floor in the region next to the corners. The central part of the wellbore floor experienced compressive stress (dark blue). The tickmarks in Figure 9b shows that the orientation of the opening mode failure plane below the borehole floor flare to either side of the borehole axis. However at the corner of the borehole floor, the orientation of failure planes is highly variable, but symmetric about the plane containing the borehole floor.

a) **b)**

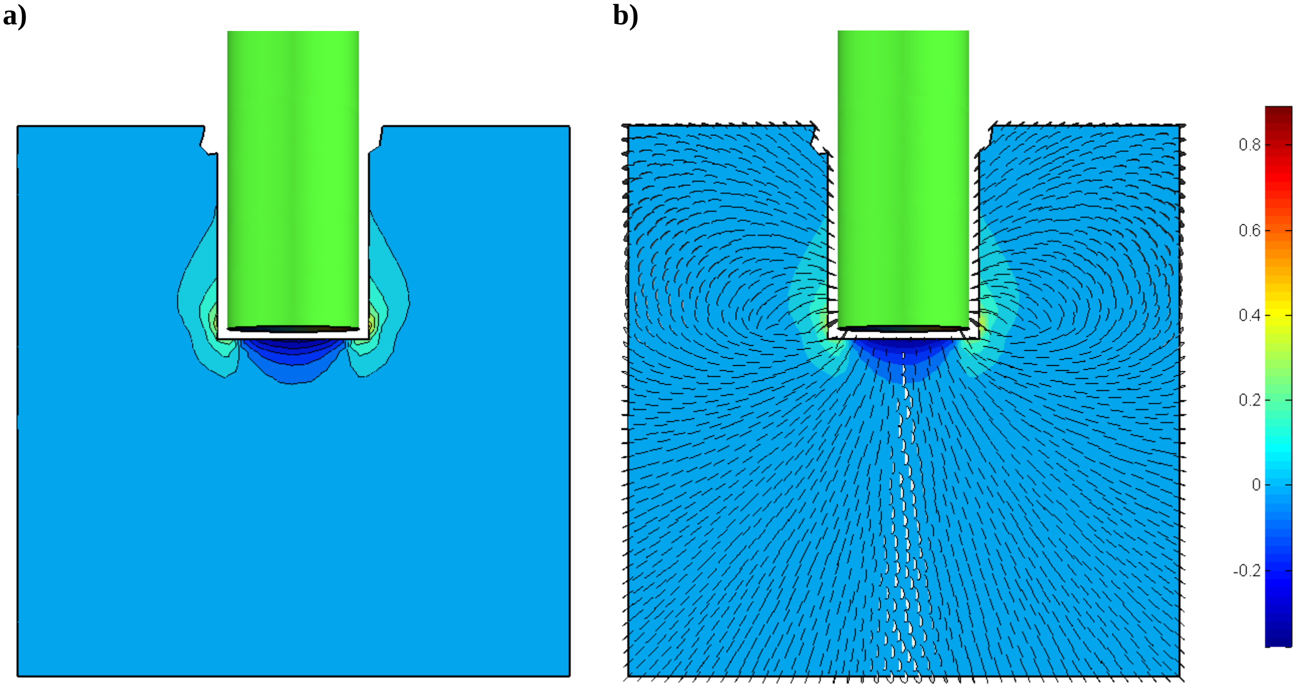

Figure 9. Effect of 1 MPa weight on bit on the stress concentration of the local principal stress S_1 at the bottom of a borehole. The color contour scale goes from -0.38 MPa (blue) to 0.89 MPa (red). b) Tickmarks representing the orientation of the opening mode failure plane normalized to S_1.

- Drilling Mud Pressure

A series of normal tractions were applied at the centroid of the triangular elements forming the walls and floor of the modeled well to simulate drilling mud pressure. The tractions were implemented with an outward direction and a magnitude of 1 MPa. Outward acting tractions correspond to the case in which the pressure of drilling mud exceeds the formation fluid pressure which "pushes" back against it. This difference in pressure is generally referred to as the differential mud pressure, *dP*, and is defined as the formation pore fluid pressure, P_p, subtracted from the mud pressure, P_m, i.e., as $dP = P_m - P_p$. The direction of these tractions are referenced to the unit outward normal of the elements discretizing the borehole floor and walls and positive magnitudes always correspond to an outward traction in which *dP* is positive whereas negative magnitudes correspond to inward acting tractions.

On the borehole walls, positive *dP* tractions add tension tangential to the walls in the $S_{\theta\theta}$ direction; while compressive stresses were generated on the two remaining directions. Note that a rotation in the direction of the local principal stresses exist when approaching the corner connecting the wall and floor of the borehole accompanied by an increase in the amplification of tension; this can be easily seen by the rotation of the tick marks and the contour of the S_1 magnitudes in Figure 10. It is important to point out that the amplification of tension on the lower section of the wall and the floor near the corners is about 2.7 times larger than that generated by the *WOB* alone in the previous example. Also note that the tension generated on the wellbore wall is perpendicular to that created by the *WOB.*

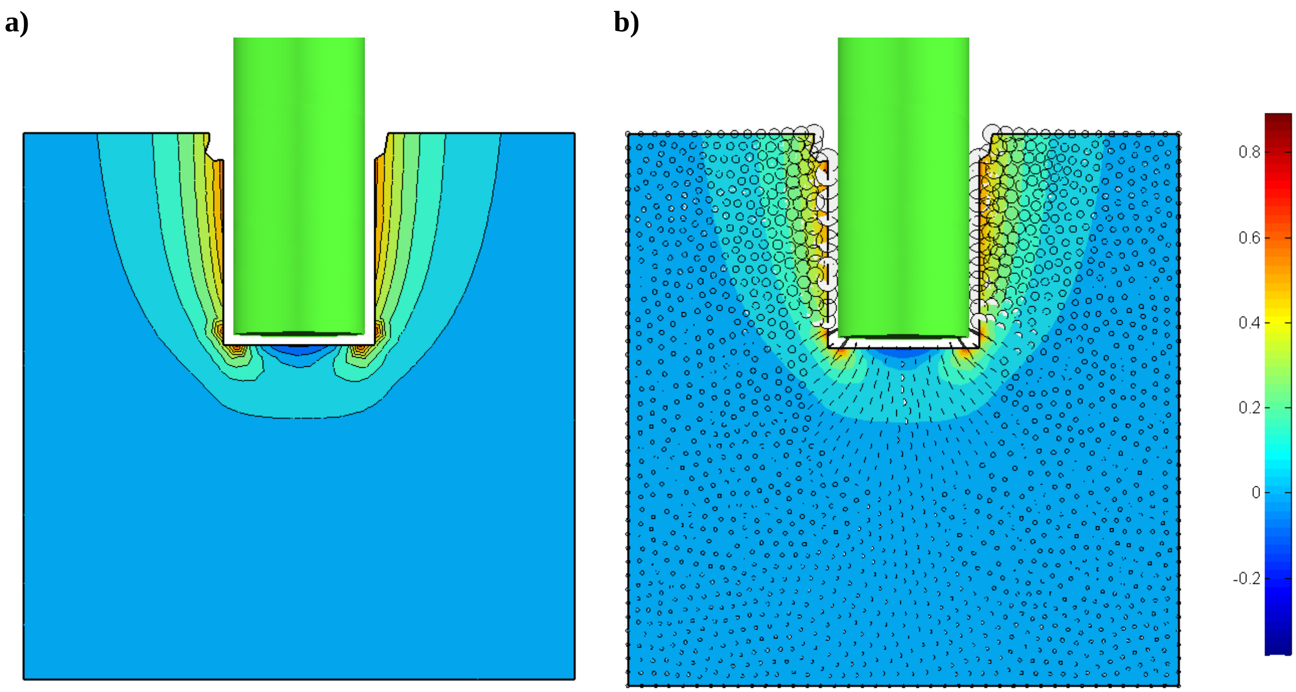

Figure 10. Effect of 1 MPa Drilling Mud Pressure on the stress concentration of the local principal stress S_1 at the bottom of a borehole. b) Tickmarks representing the orientation of the opening mode failure planes normalized to S_1. The color contour scale goes from -0.38 MPa (blue) to 0.89 MPa (red).

- Formation Pore Pressure

A series of normal tractions were applied at the centroid of the triangular elements comprising the walls and floor of the modeled borehole to simulate formation pore pressure. The tractions were implemented with an inward direction and a magnitude of 1 MPa. The central part of the floor of the borehole experienced tensile stresses in the three local principal directions, with the maximum principal local stress being in the S_{zz} direction, see Figure 11. Towards the corners, compressive stresses developed tangential to the floor and pure compression concentrated at the corner. Moving from the corner and up to the wall, compressive stresses are found in the S_{rz} and $S_{\theta\theta}$ direction, while tension develops in the S_{rr} direction; at a distance of about one radius above the corner only a compressive stress in the $S_{\theta\theta}$ direction remains. It is important to notice that yet this has been the only case where tensile stresses have been generated in the central part of the borehole floor. Also note that compared to the case with WOB and mud pressure, the pore pressure has the largest effect on the amplification of the tensile stress magnitude (red); evident since the same contour scale is used.

a) **b)**

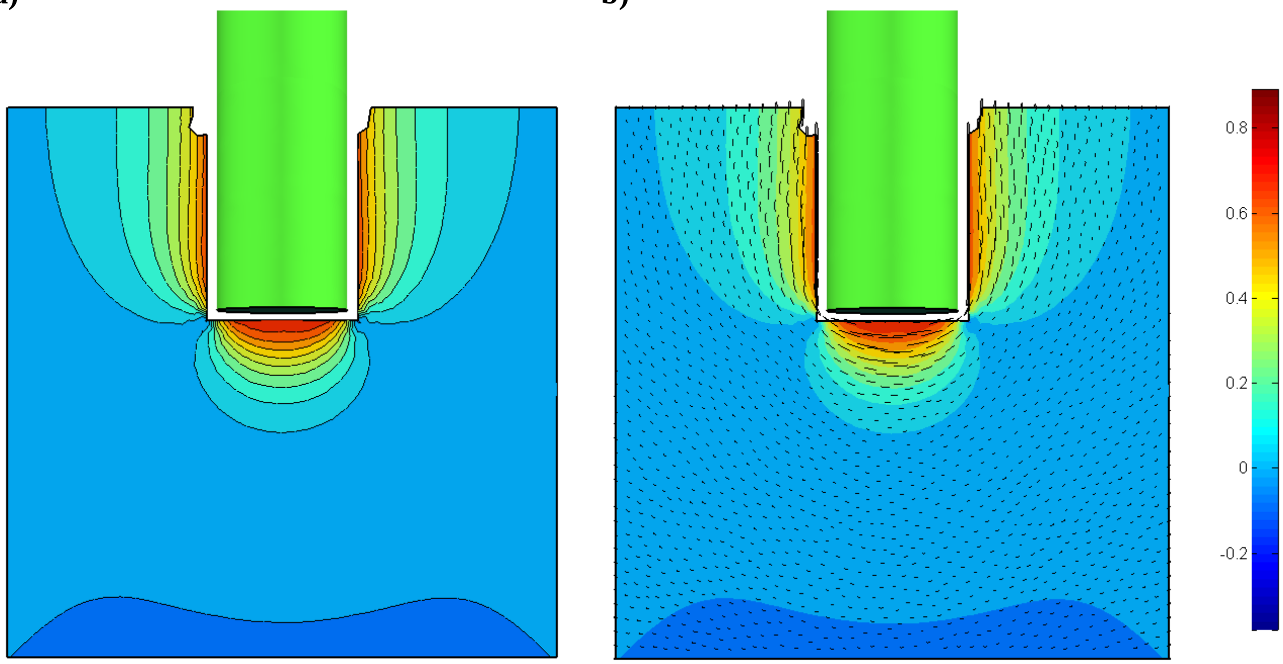

Figure 11. Effect of 1 MPa Formation Pore Pressure on the stress concentration of the local principal stress S_1 at the bottom of a borehole. a) Color contour scale is from -0.38 MPa (blue) to 0.89 MPa (red). b) Tickmarks representing the orientation of the opening mode failure planes normalized to S_1.

Although tensile stresses have been generated on the borehole walls in the last three cases (weight on bit, mud pressure and formation pore pressure) it is important to notice that their directions are perpendicular relative to each other and therefore when present simultaneously they would have a somewhat competing effect. The color contour scale goes from -0.38 MPa (blue) to 0.89 MPa (red).

- Uniform Remote Stress

A uniform compressive remote stress with magnitude 1 MPa was applied in the vertical and two orthogonal horizontal directions (S_v, S_{Hmax} and S_{hmin}), representing the extreme case in which the three principal remote stresses are equal. As it can be imagined, the effect of these three remote stresses on an empty cylindrical space such as the well creates an inward displacement of the walls and floor in which the local least compressive stress S_1 (red) develops perpendicular to the surfaces; this is in the S_{rr} direction for the case of the walls and in the S_{zz} direction for the case of the floor, see Figure 12. It is also important to point out that the local principal most compressive stress S_3 developed tangential to the bottom of the well in the S_{rr} direction and when approaching the corner it rotates to become tangential to the walls in the $S_{\theta\theta}$ direction. Although tension is not developed under these conditions the compressive stress acting in the S_{zz} direction is substantially reduced to about -0.125 MPa (red) in the central part of the borehole floor.

a) **b)**

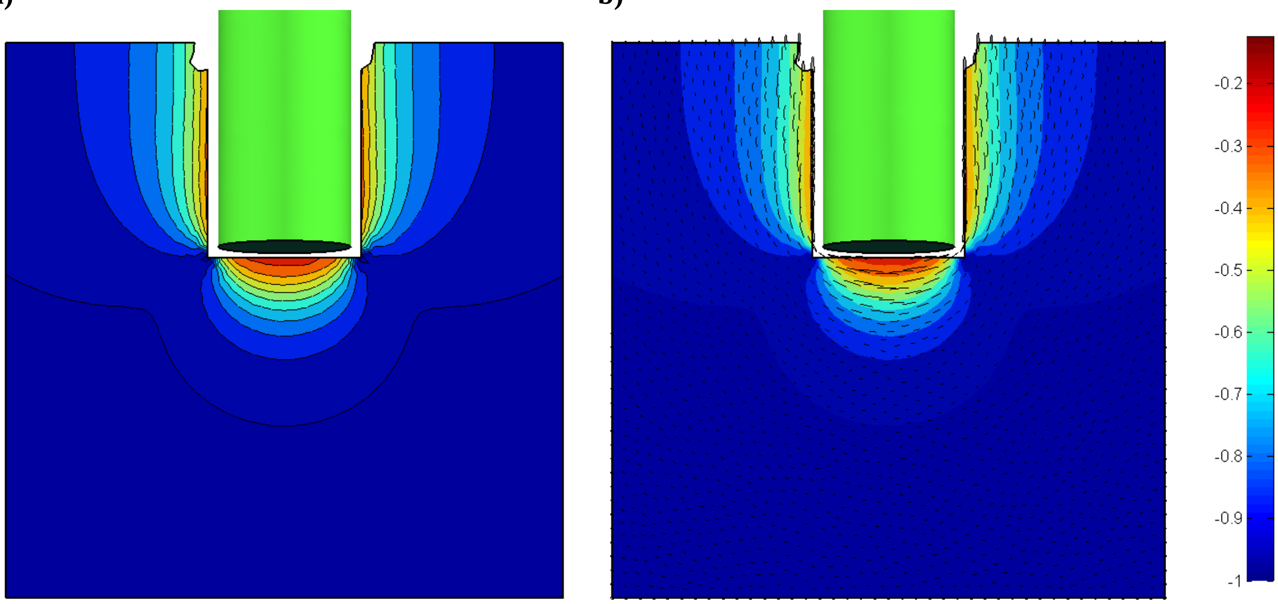

Figure 12. Concentration of the local principal stress S_1 due to uniform remote compressive Stress of magnitude 1 MPa applied in the three principal directions. b) Tickmarks representing the orientation of the opening mode failure planes normalized to S_1. The color contour scale goes from -1 MPa (blue) to -0.125 MPa (red).

- Vertical Plane Remote Stresses

A constant compressive remote stress of 1MPa was applied in the vertical direction (S_v) and on the horizontal direction parallel to the y-axis (S_{Hmax}), while the third direction in the horizontal plane parallel to the x-axis was set to zero (S_{hmin}). Figure 13 shows the concentration of the least compressive local principal stress S_1, (a) and (b) show the $S_v – S_{hmin}$ plane, while (c) and (d) show the $S_v – S_{Hmax}$ plane. The remote stress state generated compressive stresses in the three local principal directions on the wall of the borehole in the $S_v – S_{hmin}$ plane, see Figure 13a; and tensile stresses on the wall in the $S_{\theta\theta}$ direction in the $S_v – S_{Hmax}$ plane, see Figure 13c. Such amplification of the hoop stress is typical of a large horizontal differential stress and it could originate the formation of tensile fractures and breakouts on the borehole wall. When looking at the concentration of S_1 at the floor in the $S_v – S_{hmin}$ plane, tensional stress in a direction near S_{zr} appears at the corner and is amplified towards the central part of the borehole floor, also note that the two characteristic stress concentration lobes appear in the failure plane front, Figure 13 a) and b). When looking at the floor in the $S_v – S_{Hmax}$ plane, see Figure 13 c) and d), the corners remain with a tensile stress component, but this time in the $S_{z\theta}$ direction and gets amplified as one approaches the central part of the floor, this is evident by looking at the tickmarks in d). It can be concluded that a large differential stress strongly contributes to the formation of a tensile region below the bottom of the well.

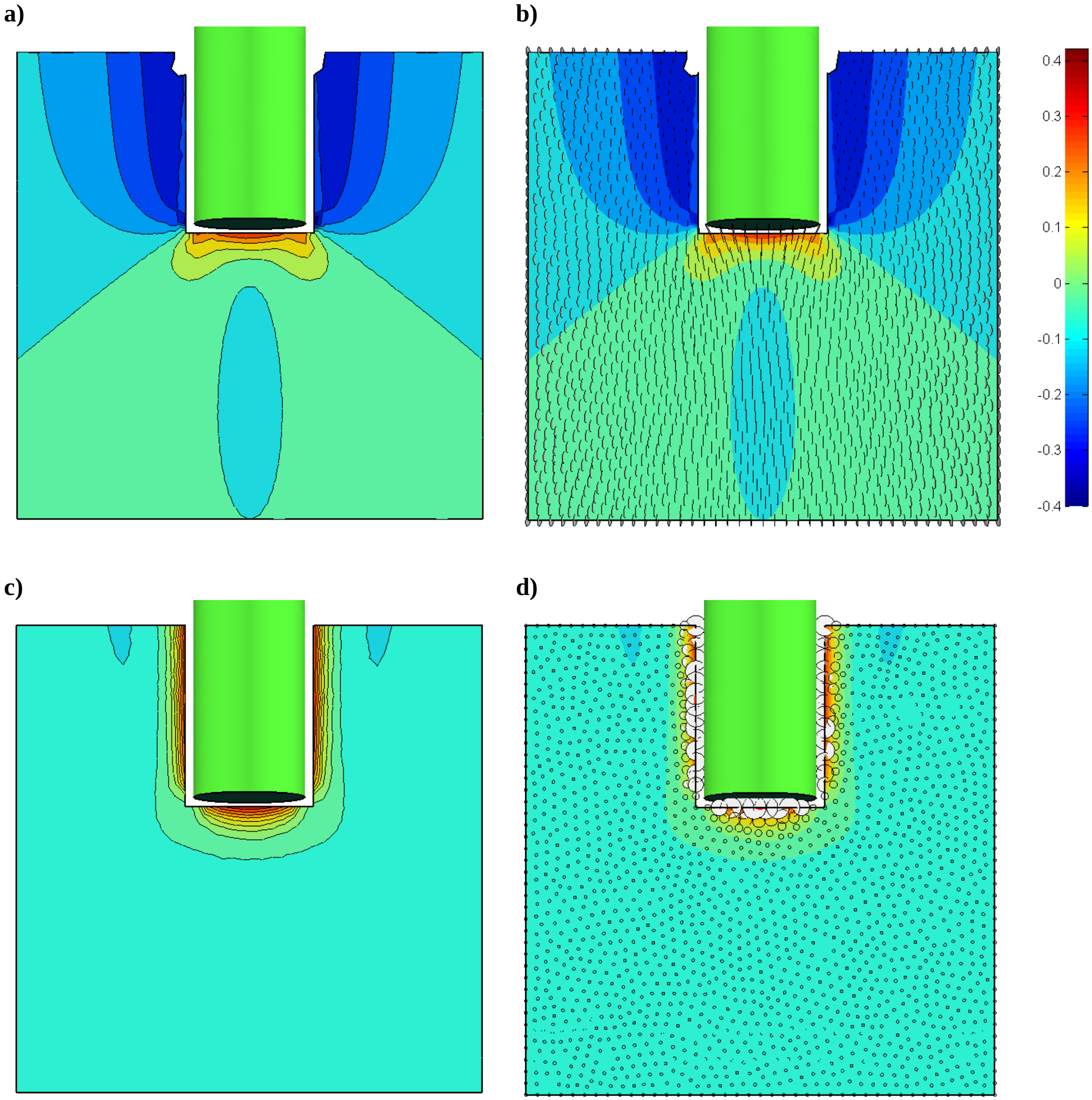

Figure 13. Concentration of the local principal stress S_1 due to remote stresses S_v and S_{Hmax} of magnitude 1 MPa applied in a vertical plane. a) and b) show the $S_v - S_{hmin}$ plane. c) and d) show the $S_v - S_{Hmax}$ plane. Tickmarks in b) and d) represent the orientation of the opening mode failure planes normalized to S_1. Color contour scale goes from -0.4 MPa (blue) to 0.42 MPa (red).

- Horizontal Plane Remote stresses

A constant compressive remote stress of 1MPa was applied on the two horizontal directions S_{hmin} and S_{Hmax} parallel to the x and y-axis, while the remote stress in the vertical direction (S_v) was set to zero. Corresponding to the extreme case where the two horizontal stresses are equal to each other and the vertical stress is negligible compared to the first two. Since the stress concentration at the bottom of the well is symmetric in both principal planes only one of them is shown in Figure 14. The remote stress state generated local tensile principal stresses on the wall of the borehole in the direction S_{rz} that were amplified towards the bottom of the well. There was a subtle stress rotation at the corner in which the local principal tensile stress was reduced and became parallel to the S_{zz} direction. Compressive stress in all local principal directions was developed at the bottom of the well in the region near the corners, while the central part of the floor experienced a tensile stress in the S_{zz} direction. This combination of compression towards the corners and tension at the central part of the floor was generated by the deformation of the floor from buckling into a slight *w* shape.

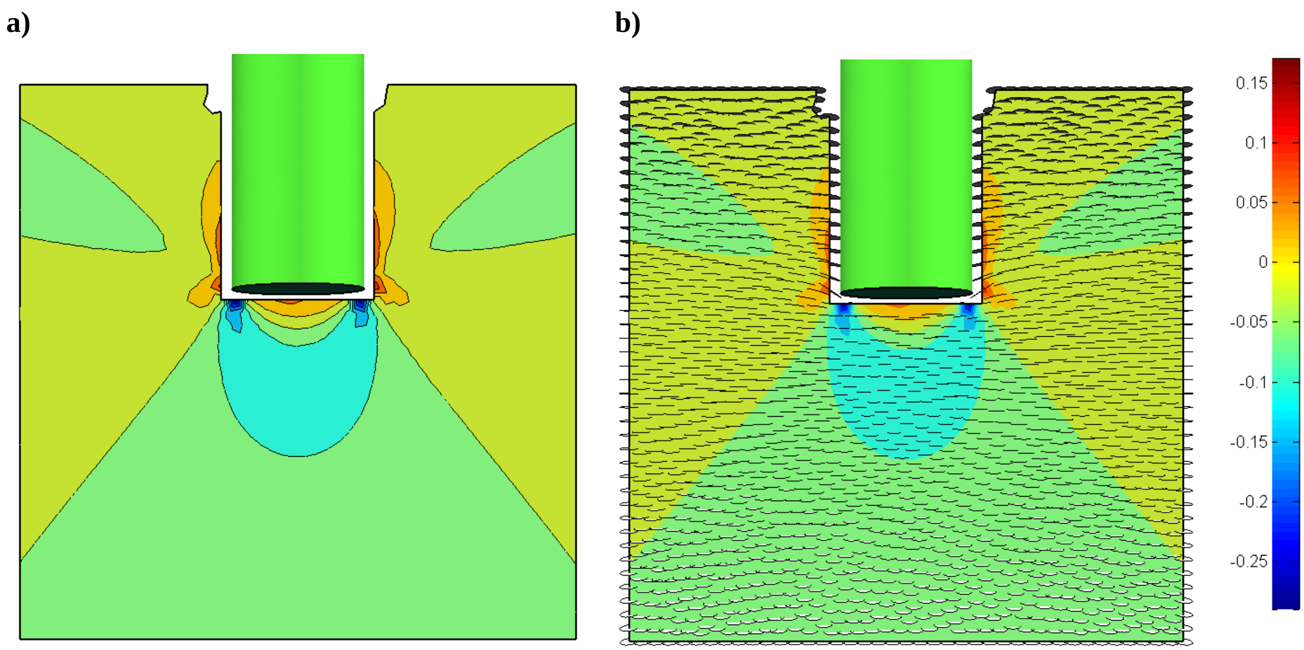

Figure 14. Concentration of the local principal stress σ_1 due to remote stresses S_{hmin} and S_{Hmax} of magnitude 1 MPa applied in a horizontal plane. Tickmarks in b) represent the orientation of the opening mode failure planes normalized to S_1. The color contour scale goes from -0.29 MPa (blue) to 0.17 MPa (red).

The boundary conditions were shown to play a strong role in the concentration of tensile stresses below the borehole floor. Therefore, a sensitivity analysis determining how key physical properties and boundary conditions such as Poisson's ration, excess mud pressure and weight on bit impact the maximum concentration of stress (most tensile) near a borehole floor was in order and is presented next.

3.2.1 **Methods**

The vertical flat-bottomed well was modeled under the remote stress conditions determined on well 58A-10 while the individual boundary conditions were varied over a range to quantify their impact on the stress concentration. The stress state in 58A-10 is best constrained at a true vertical depth below ground level of 2326.5 m from previous work by Davatzes and Hickman (2006; 2007). At this depth the vertical principal stress was estimated to be -58.6 MPa assuming an average overburden density of 2.57 g/cc and the formation pore pressure equal to 19.2 MPa by integrating the density of water taking into account its equation of state and the temperature profile in the surrounding formation (see Figure A 1and Figure A 2 in Appendix A).Table 3 summarizes the conditions used throughout this work.

Table 3.Conditions used derived from analysis of well 58A-10 Coso Geothermal Field (Davatzes and Hickman, 2006; Davatzes and Hickman, 2007).

Parameter	**Magnitude**	**Notes/Source**
Borehole radius	0.0794 m	Mud Log
MD (below GL)	2331.1 m	Mud and Geophysical logs
TVD (below GL)	2326.5 m	Deviation survey in geophysical image logs (Davatzes and Hickman, in press)
S_V	-58.6 MPa	Integrated from rock density (Davatzes and Hickman, 2006; 2007)
S_{Hmax}	-100.5 MPa	Constrained by Uniaxial Rock Strength measured by Morrow and Lockner (2005), breakout width (Davatzes and Hickman, 2006; 2007) and Shmin from mini-hydraulic fracturing experiment (Davatzes and Hickman, 2007)
S_{hmin}	-37.9	Mini-hydraulic fracturing experiment (Davatzes and Hickman, 2007)
P_P	19.2 MPa	This represents the modern formation fluid pressure (Note, this is distinct from the pre-production fluid pressure used in the analysis of Davatzes and Hickman (2006, 2007) provided in the Appendix).
P_m	21.68 MPa	Magnitude estimated from Mud Log at time drilled. Pm = **ρ** g z
WOB	5.12 MPa	Mud log: WOB [Pa]= $WOB^{mud\ log}$*4.0823318493/(pi*r^2) $WOB^{mud\ log}$ = mud log weight on bit [lb] = 25,000 lb lb to N conversion = 4.0823318493 N/lb pi*r^2 = area of borehole of radius r [m]
μ_s	0.8	Result of rock mechanics analysis by Morrow and Lockner (2005) and summarized in Davatzes and Hickman (2007). Note that Byerlee friction indicates most rock forming minerals range from 0.6 to 1.

ν	0.25	Average Poisson ratio of values in the Coso Geothermal Field measured by Morrow and Lockner (2005) of representative rock types including granites and diorites in the Coso Geothermal Field (summarized by Davatzes and Hickman, 2007). Also consistent with granitic and dioritic rocks in general (Jaeger et al., 2007).

The maximum concentration of stress in two different regions was determined, (1) below the borehole floor and (2) along the borehole walls near the floor. In all subsequent figures shown, the magnitude of the maximum local principal stress S_1, below the borehole floor is indicated by a hollow red diamond; S_1 along the borehole wall in the vicinity of the floor is indicated by an inverted green triangle, and the maximum S_1 taking both regions into account with a blue circle. All tensile local stresses found in the model were also plotted as gray rectangles to ensure that a region of tensile stress indeed exists and the maximum stress found is not a local anomaly.

For the sensitivity analysis of Poisson's ratio, eight different models were run with values of Poisson's ratio ranging from 0 to 0.5 representative of most rocks (Jaeger, Cook, & Zimmerman, 2007). Eleven cases ranging from 0 to10 MPa were run for the analysis of *WOB* at uniform interval increments of 1 MPa. 38 cases ranging from -20 to 25 MPa were run to evaluate the impact of *dP* at conditions where zero drilling mud pressure is found to that where the mud pressure exceeds double the formation pore pressure. The results of the sensitivity analysis are presented next.

3.2.2 **Results**

The effect of Poisson's ratio on the maximum concentration of stresses in the vicinity of a well floor is shown in Figure 15. The blue semi-transparent rectangle indicates the typical range of Poisson's ratio for rock; the red dotted line shows a Poisson's ratio of 0.25 representative of rock penetrated by borehole 58A-10, and the value used in all models in this study. Neither excess pressure nor weight on bit (*WOB*) were taken into account in this model to isolate the impact of Poisson's ratio. The analysis suggests that σ_1^{max} is relatively insensitive to Poisson's ratio and that for these boundary conditions it remains constant and relative compressive below the borehole floor. In contrast, this analysis indicates that for increasing values of Poisson's ratio the maximum local magnitude of σ_1^{max} along the wall of the borehole near the floor also becomes more tensile. The grey rectangles correspond to a whole region experiencing tension along the walls of the borehole near the floor.

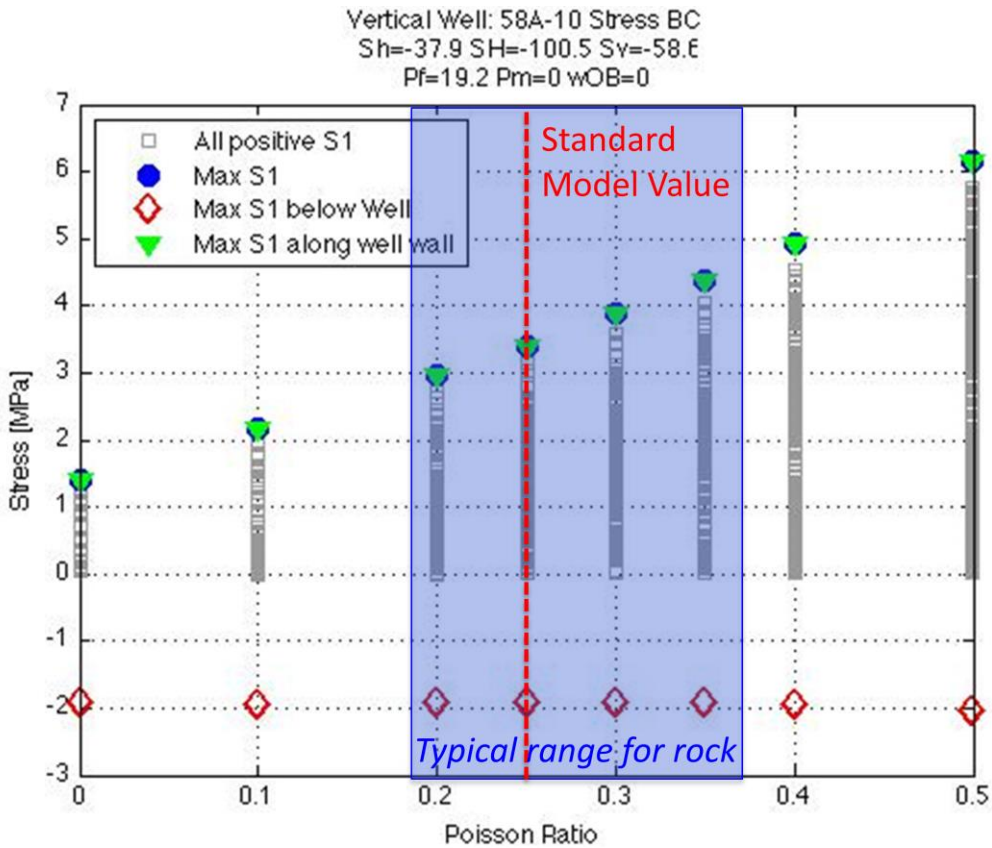

Figure 15. Sensitivity analysis of σ_1^{max} below the borehole floor and along the adjacent borehole walls to Poisson's ratio.

The impact of weight on bit on the concentration of the local principal stress σ_1 along the borehole walls near the borehole floor and below it is illustrated in Figure 16. The red dotted line indicates the magnitude of the weight on bit used in borehole 58A-10 in a depth were petal-centerline fractures were observed and the stress state is well-constrained. The general trend indicates that as *WOB* increases so does σ_1 below the borehole floor, therefore facilitating the nucleation of petal-centerline fractures. Note that the maximum magnitude of tension is concentrated along the walls of the borehole as indicated by the coinciding overall maximum $\sigma_1$with the local maximum σ_1 (blue circles and green inverted triangles respectively). It is important to note that the concentration of σ_1 below the floor dramatically increases passed a *WOB* of 3 MPa, and generates tensile stresses after a value of 8 MPa. The population of locations with tensile σ_1 is indicated by the grey rectangles corresponding to a substantial volume surrounding the floor and walls of the borehole subjected to tension. Insights from Figure 9 and preliminary visualization of these models suggest that the tensile region is localized near the corner of the borehole and might thus act as a nucleation site form Mode I fracture.

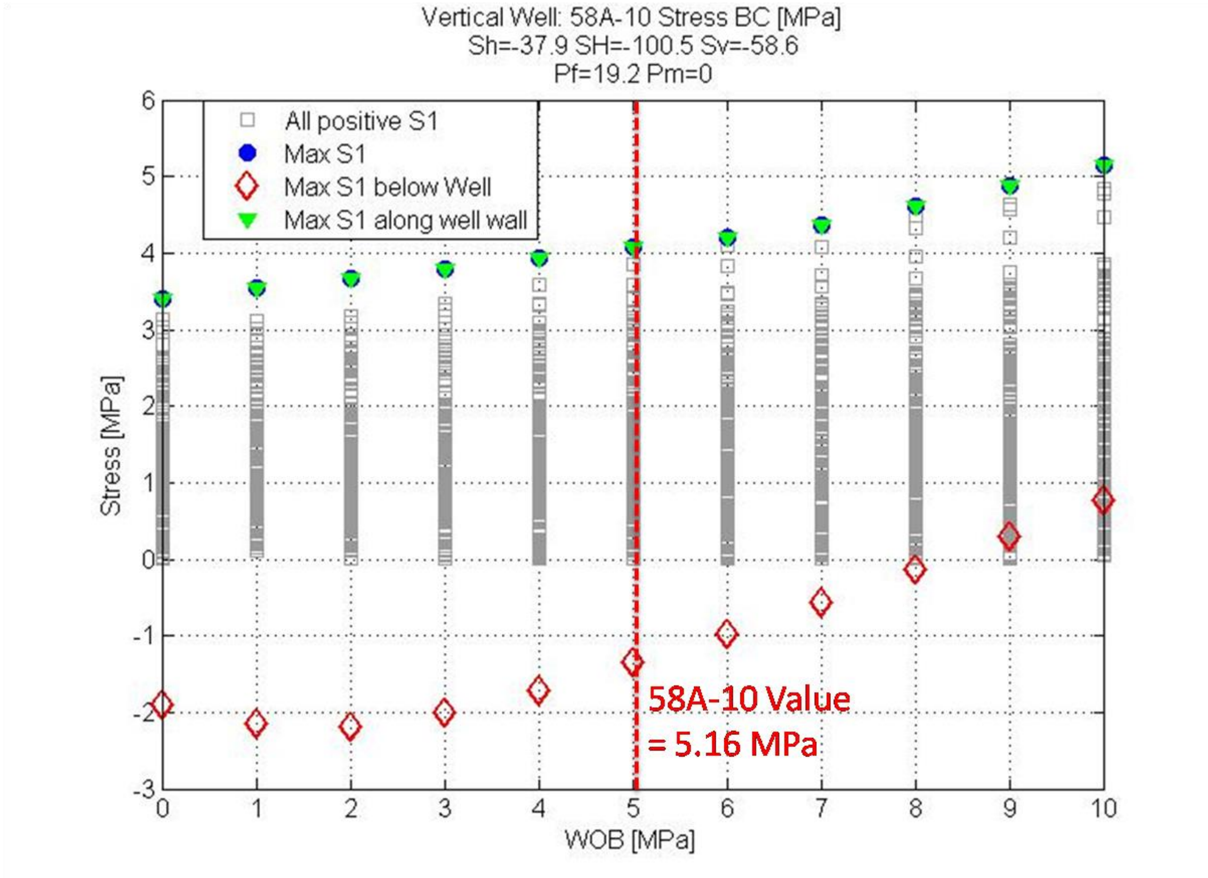

Figure 16. Sensitivity analysis of the concentration of local principal stress around the borehole floor to Weight on Bit (WOB).

The magnitude of σ_1^{max} is highly sensitive to the balance between mud pressure and fluid pressure represented by $dP=P_m-P_p$ (Figure 17). The minimum magnitude of σ_1^{max} below the borehole floor occurs in the region where the formation fluid pressure is only slightly lower than the drilling mud pressure; as the *dP* becomes negative, tension below the borehole floor is achieved and rapidly increases. Increasingly positive *dP* also promotes increasingly tensile σ_1^{max}, although less rapidly. This is consistent with effects of drilling mud pressure and formation mud pressure on σ_1 illustrated in Figure 10 and Figure 11 respectively. However, in cases where the mud pressure remains close to the formation pore pressure, compressive σ_1^{max} is promoted below the borehole from approximately -1 to 5 MPa of *dP*. In contrast, the walls of the borehole are always in tension for the simulated 58A-10 conditions. The over-all sensitivity to *dP* is similar for both the borehole floor and walls, although excess mud pressure more strongly promotes tension along the borehole walls as a hoop stress. For negative *dP*, the magnitude of tension in the two regions quickly converge and similarly promote Mode I fracture in planes parallel the borehole surfaces, with a more complex pattern at the corners.

Note that during the drilling of well 58A-10 the differential pressure only ranged between zero and approximately 3 MPa. This coincides with the range with the least impact on the local magnitude of σ_1^{max} both below the borehole floor and along its walls, although compression below the borehole floor is slightly enhanced. The red dotted line represents a *dP*=2.48 MPa which is the drilling pressure reported at the depth where a large population of petal-centerline fractures are visible in image logs of borehole 58A-10. It is important to notice that under the remote stress state modeled, the maximum local concentration of stress along the borehole floor at the bottom of the borehole is always tensile for all values of *dP*. Table 4 summarizes the results obtained in this section.

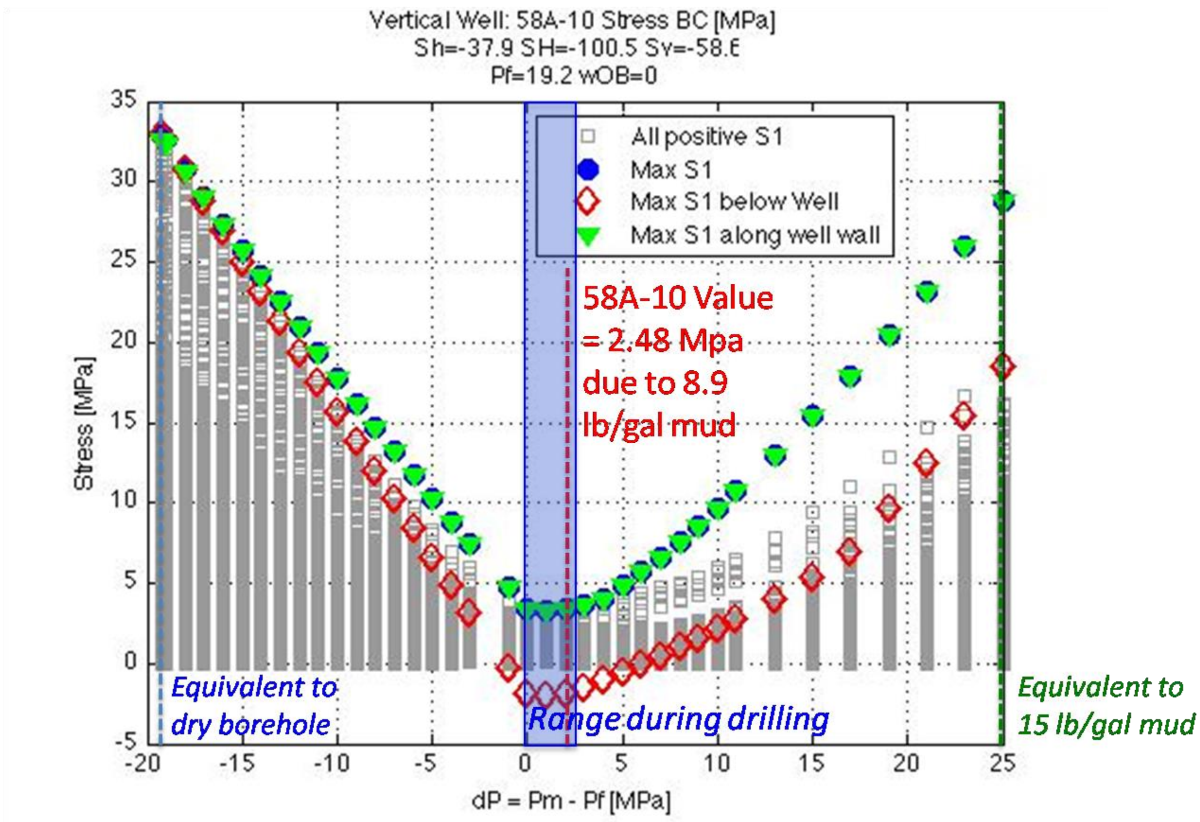

Figure 17. Sensitivity of the concentration of local principal stress around the borehole floor to dP.

Table 4. Summary of effect of the different boundary conditions on the concentration of stresses near the borehole floor (58A-10 solid stresses and fluid pressure).

Boundary Condition	**Impact on the generation of tension below the borehole floor**	**Impact on the generation of tension on the walls near the floor**
Poisson's ratio	NO	YES
dP	YES (especially at small dP)	YES (always in tension)
WOB	YES	YES (always in tension)

3.3 Impact of remote stress boundary conditions on stress concentration due to a vertical well

3.3.1 Methods: Fault Regimes and Permissible Stresses on Earth

The stress concentration due to the walls and the floor of a borehole depends on the remote principal stresses acting on the rock while the borehole was drilled. Townend and Zoback (2000) argue that the potential combinations of remote principal stresses in the Earth's shallow, brittle crust are limited by the coefficient of sliding friction of existing fractures. In this section the evidence and theory supporting this hypothesis and their relationship to different faulting regimes are reviewed as a necessary constraint on exploring the conditions that could produce petal-centerline fractures.

The surface of the Earth is traction free and therefore cannot sustain shear stress; thus it acts as a principal plane containing two principal stress directions while the third principal stress direction is orthogonal to the Earth's surface. This implies that near the Earth's surface one principal stress is vertical, S_V, and has a magnitude equal to the weight of overlying rock resulting in increasingly compressive magnitudes with increasing depth (labeled S_V in Figure 18). Compressive brittle failure of rock is governed by the Mohr-Coulomb failure envelope (Jaeger et al., 2007) which limits the difference between the maximum and minimum principal stresses, σ_1 and σ_3 respectively (tensile stress positive), for any magnitude of effective σ_3'. If that limit is exceeded, the rock breaks to form a new fault or slip occurs on an established fault that relieves elastic strain and thus limits the differential stress. As a result, all three principal stresses become increasingly compressive with depth (Figure 18, left column). This limit is defined in a Mohr Circle construction of normal versus shear traction as a line of constant slope (Figure 18, middle column). Pre-existing surfaces in rock typically slip when the ratio of shear to normal traction defining the coefficient of sliding friction, μ_s, are in the range of 0.6 to 1.0 (Byerlee, 1978; Lockner et al., 2003). Because fluid pressure, P_p, will act to push fracture surfaces apart, an effective normal stress must be defined as the addition of the fluid pressure to the normal stress to determine failure. Thus, a change in pore pressure would affect the size and position of the Mohr circle, shifting it to the right as pore pressure increases. Similarly, failure of intact rock shows a pressure dependence, but overall rock strength is increased by the cohesion of the intact rock. Because not actual surface exists to accommodate deformation until failure, the failure envelope is referred to as the coefficient of internal friction, μ_i (Figure 3, middle column). The extremes of the Mohr Circle are defined by the maximum and minimum principal stress and all possible combinations of shear and normal tractions are defined along the circumference of the circle. Well-oriented faults maximize the ratio of shear to normal tractions and if present will always slip before new faults are formed.

Anderson (1951) recognized that which principal stress is vertical dictates the type of faulting regime (Figure 18, right column); normal faulting occurs when the $S_V = \sigma_3$, reverse faulting occurs when $S_V = \sigma_1$, and strike-slip faulting occurs when $S_V = \sigma_2$. To facilitate the geographic reference frame, the remaining two horizontal principal stresses are designated the maximum compressive principal stress, S_{Hmax}, and the minimum compressive principal stress, S_{hmin}. Consequently, in normal faulting $S_v > S_{Hmax} \geq S_{hmin}$, in reverse faulting $S_{Hmax} > S_{hmin} \geq S_v$, and in strike-slip faulting $S_{Hmax} > S_v \geq S_{hmin}$.

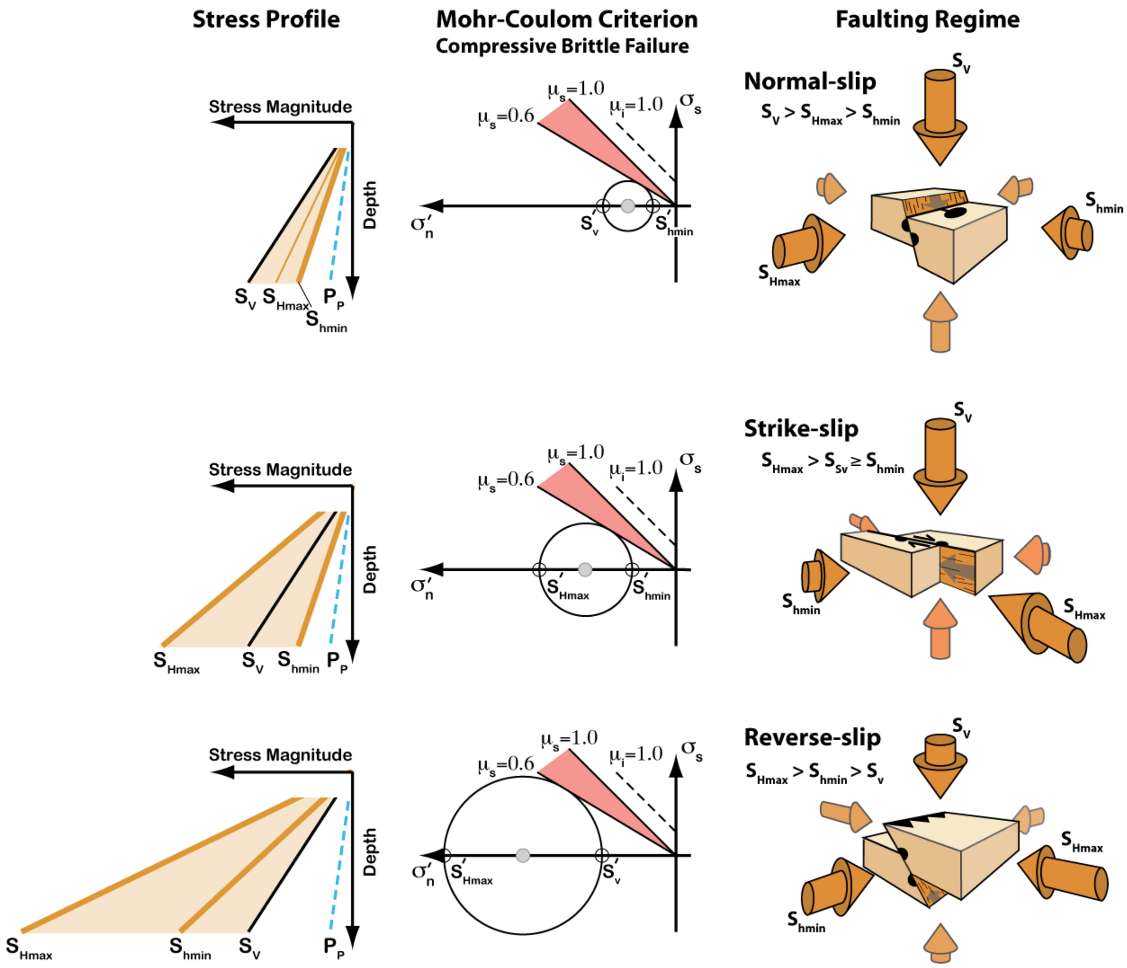

Figure 18.Column 1: Stress profiles with depth, from top to bottom, where $S_V = \sigma_3$ corresponding to normal faulting, $S_V = \sigma_2$, corresponding to strike-slip faulting, and corresponding to reverse faulting $S_V = \sigma_1$. Column 2: The range in magnitudes of the minimum and maximum effective principal stress magnitudes (effective stress is indicated by the prime) are limited by rock strength for intact rock or by the frictional resistance to sliding on established fracture surfaces defining the Mohr-Coulomb failure envelope. For the depth range penetrated by wells, the resulting failure conditions are pressure dependent equal to a constant ratio of normal to shear traction between 0.6 and 1.0 (Lockner et al., 2003). Column 3: In the simple case, faulting accommodates plane strain deformation with extension in the direction of σ_1, which is the least compressive (i.e., most tensile) principal stress in the tensor stress convention where tension is positive. To facilitate the geographic reference frame the principal stress are defined for each "faulting regime" as the vertical stress, S_V, the maximum compressive horizontal stress, S_{Hmax}, and the minimum compressive horizontal stress, S_{hmin}.

In the shallow, brittle crust, compiled measurements of remote stress magnitudes at depth have shown that the difference between maximum and minimum principal stress ($\sigma_1 - \sigma_3$) is limited by the frictional strength of established optimally oriented faults (Townend & Zoback, 2000). As the magnitude difference between the maximum and minimum principal stresses increases, i.e. S_v and S_{hmin} in normal faulting, the most favorably oriented faults will slip as their frictional strength is reached and no further differential stress increase would be possible; see Figure 19. The inference is that the ubiquitous occurrence of faults and other discontinuities of different size and orientation visible in outcrops and core or image logs from boreholes provide established surfaces to localize slip. As discussed, frictional sliding on a plane occurs when the ratio of shear to effective normal stress reaches the frictional limit, μ_s, to give the expression:

$$\tau_{critical} = \mu_s(\sigma_N + P_p) \qquad (4)$$

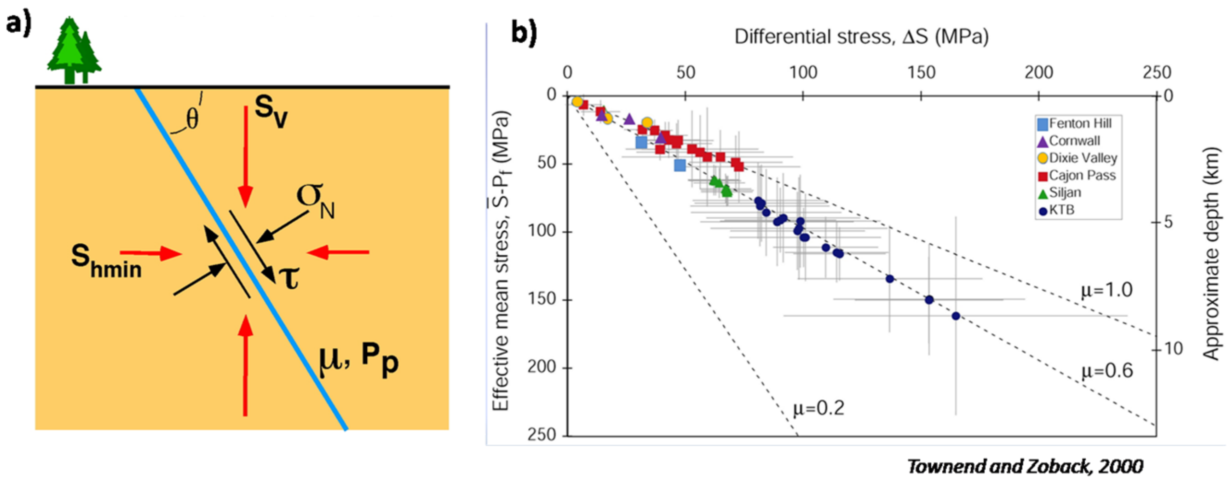

Figure 19. a) Frictional sliding on well-oriented fault plane (θ ~ 60°) in normal faulting. b) Coefficient of friction measured by Townend and Zoback in different faulting environments and rock types confirming Byerlee's law.

This is represented by a Mohr circle touching a frictional failure envelope of slope μ_s. According to Byerlee's law, the coefficient of friction in the Earth's upper crust ranges between 0.6 and 1.0. (Townend & Zoback, 2000) confirmed the range of stress magnitude predicted, this range of friction is consistent with the measured stress state in a wide range of faulting environments and most rock types (with a few exceptions, e.g., weak clays) through numerous borehole measurements; see Figure 19b. The maximum to minimum compressive principal stress ratio at which a fault optimally oriented to maximize the shear to effective stress ratio at the frictional limit for the different faulting environments can be expressed as follows (Jaeger & Cook, Fundamentals of Rock mechanics, 1979):

Normal Faulting $$\frac{\sigma_3'}{\sigma_1'} = \frac{S_v + P_p}{S_{hmin} + P_p} \leq [(\mu_s{}^2 + 1)^{1/2} + \mu_s]^2 \qquad (5)$$

Strike-slip Faulting $$\frac{\sigma_3'}{\sigma_1'} = \frac{S_{Hmax} + P_p}{S_{hmin} + P_p} \leq [(\mu_s{}^2 + 1)^{1/2} + \mu_s]^2 \qquad (6)$$

Reverse Faulting $$\frac{\sigma_3'}{\sigma_1'} = \frac{S_{Hmax} + P_p}{S_v + P_p} \leq [(\mu_s{}^2 + 1)^{1/2} + \mu_s]^2 \qquad (7)$$

Note that the ratio between σ_3' and σ_1' is determined by the coefficient of friction μ_s regardless of the faulting environment and therefore as S_V increases with depth so do S_{Hmax} and S_{hmin}, this becomes evident in Figure 18. The permissible range of principal stresses in the crust can be illustrated as a stress polygon for given depth, pore pressure, and coefficient of sliding friction

(Zoback, Mastin, & Barton, 1987) (Figure 20). The polygon is divided into the three faulting regimes illustrating the ranges of normal, reverse and strike-slip faulting assuming the Mohr-Coulomb frictional failure theory and Anderson's fault classification. Note that since S_{Hmax} is always greater or equal than S_{hmin} all permissible stress states are above a diagonal line of unit slope. If the stress state falls on the boundary of the polygon, it is said to be in frictional failure equilibrium. The size of the stress polygon depends on the coefficient of friction and the pore pressure. Increased frictional strength or decreased pore pressure increase the size of polygon allowing a greater range of frictionally stable stress states. Thus, the stress polygon constrains the possible ranges of values of the maximum horizontal principal stresses (Zoback M. D., et al., 2003).

Assuming a constant value of friction and an incompressible fluid as in Figure 18 implies that the potential range in magnitudes of the three principal stress components scale linearly with depth. This relationship is generalized by normalizing the horizontal principal stresses by the vertical stress associated with a chosen depth, thus providing a succinct summary of the scaling of remote principal stress components.

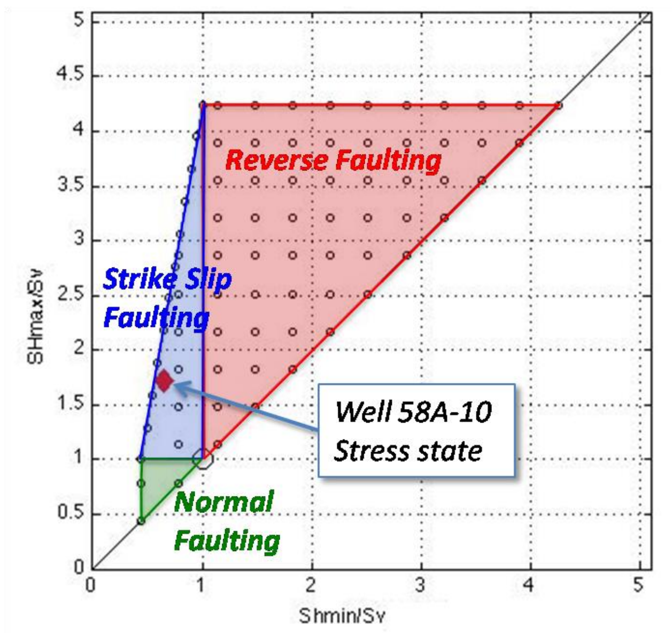

Figure 20. Stress Polygon defining the permissible stress states in the Earth's crust using a coefficient of friction of 1.0. Red diamond represents the stress state in well 58A-10 in the Coso Geothermal Field at a true vertical depth of 2326.5 m for a formation pore pressure equal to 19.2 MPa and weighted average rock density of 2.57 g/cc.

This section explores the maximum concentration of local principal stress, S_1, near the walls and floor of a borehole subjected to the frictionally permissible range of stress states and its importance relative to other boundary conditions (e.g., Table 3). For this study, a coefficient of sliding friction (μ_s=1) equal to 1 is used to constrain the range of permissible stress states in the shallow brittle crust accessible by modern boreholes (Figure 20), defining a stress polygon constructed from equations (5),(6 and(7. This μ_s lies at the extreme of Byerlee Friction (Byerlee, 1978; Lockner & and Beeler, 2003) and allows the largest possible range in stress states, thus ensuring a complete exploration of permissible remote stress boundary conditions.

Within the stress polygon 76 sample states (represented by dark circles in Figure 20) were simulated and form the basis for contouring the sensitivity of tensile stress to the remote stress boundary conditions.

In the modeling effort, non-normalized magnitudes were used that represent true *in situ* stress conditions at which petal-centerline fractures were identified in image logs (Davatzes and Hickman, in press). In addition, the other major constraint on the range of remote stress boundary conditions is the fluid pressure (see section 3.2.1) since frictional resistance to slip depends on the effective normal stress. As noted previously, these correspond to the solid stresses and fluid pressure estimated for well 58A-10 at 2326.5 m Measured Depth below Ground Level (Rose, et al., 2006) (summarized in Table 3). The red diamond in the Strike-slip faulting regime shows the stress state in well 58A-10.

3.3.2 **Results: Reference stress concentration on walls of borehole 58A-10**

For reference, the Kirsch solution (Equations(1,(2 and(3) was used to calculate the stress concentration along a vertical borehole subjected to the stress state found in Coso well 58A-10 (Table 3) including implementation of the corresponding solid stresses, pore pressure, and mud pressure. Attributes of the stress concentration resulting from the 58A-10 stress state are discussed in Appendix C. The maximum σ_1 magnitude was then evaluated for each of the 76 stress states in Figure 21 and contoured defining a map of the local σ_1^{max} dependence on stress state (Figure 21). In the resulting contour map, red tones show positive (tension) magnitudes of the σ_1^{max} at the wall, while the rest of the tones show more negative (compression) magnitudes of the local σ_1^{max}. The thick white contour line demarcates the region of tension from the region of compression. Note that this result indicates that no tensile fractures would appear on the wall of a borehole located in a normal faulting region, suggesting the horizontal differential stress (S_{Hmax}-S_{hmin}) would never become sufficient to generate tension in the wall of a vertical well at this depth ($\sigma_{\theta\theta}$ component). On the other hand tension is found in the strike slip faulting and reverse faulting regimes with higher horizontal differential stress (S_{Hmax}-S_{hmin}) (upper left side of the polygon).

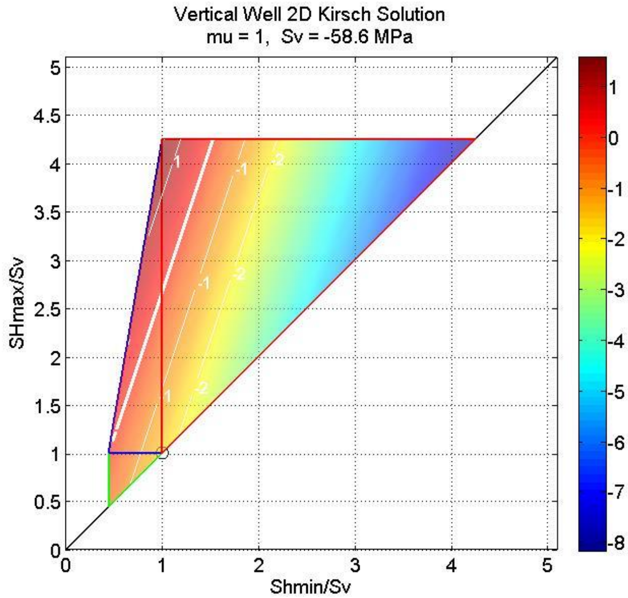

Figure 21. Stress Polygon contouring the Kirsch solution for maximum stress, σ_1^{max}, along the borehole walls. White contour lines are 1 MPa increments.

This analysis intentionally neglects the potential impact of cooling and thermal contraction of the borehole walls by circulating drilling fluids or post drilling injection on the local stress state. This cooling is insignificant at the advancing floor of the borehole due to the limited exposure time of that surface (Zoback et al., 2003; Zoback, 2007). It is neglected here to facilitate a more direct comparison to the analysis of bottom-hole stress concentration presented below. Consequently, this provides a means of evaluating the differences between the stress state at the bottom of a borehole and the simpler 2-D case, but more importantly reveals the potential impact of mis-interpreting petal centerline fractures formed below the borehole floor as tensile fractures formed in the borehole wall. Since cooling in borehole 58A-10 was as much as ~150°C at the model depth, it would significantly contribute to tension parallel to the borehole wall due to thermal contraction promoting tensile fracture of the borehole wall and correspondingly expand the region of tension in Figure 21.

3.3.3 Results: Stress concentration in vicinity of the floor of 58A-10 borehole

The local σ_1^{max} in the vicinity of the borehole floor was evaluated using the well mesh developed in Section 3.1.2 and subjected to the 76 stress states previously discussed (Figure 20). The process was repeated to quantify the impact of local boundary conditions including *dP* and *WOB* as well as their combination (Table 3). Each model output was searched using a routine in Matlab to identify σ_1^{max} below the floor of the borehole and on the adjacent borehole wall. These two regions of the borehole were selected since the main focus of this work is to simulate the most tensile stress magnitude as a necessary criterion for nucleation of Petal-centerline fractures. Results for each location are contoured to map the dependence of the stress concentration on the remote stress state and local boundary conditions. Although the right hand side of the figures presented show the maximum stress concentration on the wall in the vicinity of the borehole floor subjected to different stress states, these results are not expected to match those previously obtained using the Kirsch solution, since the latter one assumes a cylindrical hole in an infinitely long elastic material. Instead, these results thus represent the impact of the borehole floor on its *adjacent* walls, which do not strictly conform to 2D case illustrated in Figure 21. For the purpose of this set of analyses the modeled borehole is vertical; although in reality it is deviated 4.2° from vertical (the role of deviation is the subject of a subsequent section).

Figure 22 maps the variation in σ_1^{max} near the bottom of a borehole due to the impact of the effective remote stresses alone with boundary conditions on the borehole surfaces set to dP = 0 MPa and WOB = 0 MPa. The left side of the figure shows the local σ_1^{max} below the borehole floor. Only a very small fraction of the stress polygon corresponding to low mean stress is associated with tension; therefore, this figure reveals that petal-centerline fractures below the floor of the borehole would only take place in normal to strike-slip faulting regimes. The right side of Figure 22 shows the maximum concentration of stress near the walls above the floor of the borehole in this set of simulations. The thick white contour line representing the transition from tension to compression spans all the three different faulting regimes, indicating that with the remote principal stresses in the absence of excess mud pressure and no weight on bit are sufficient to induce tension and thus tensile fractures. Note that the transition from tension to compression along the borehole wall in this bottom-borehole position shows significant curvature not present in Kirsch solution (Figure 21). This suggests that for this vertical borehole, tensile fractures are expected in a much larger proportion of the reverse faulting regime, although still minimizing mean stress and maximizing horizontal differential stress.

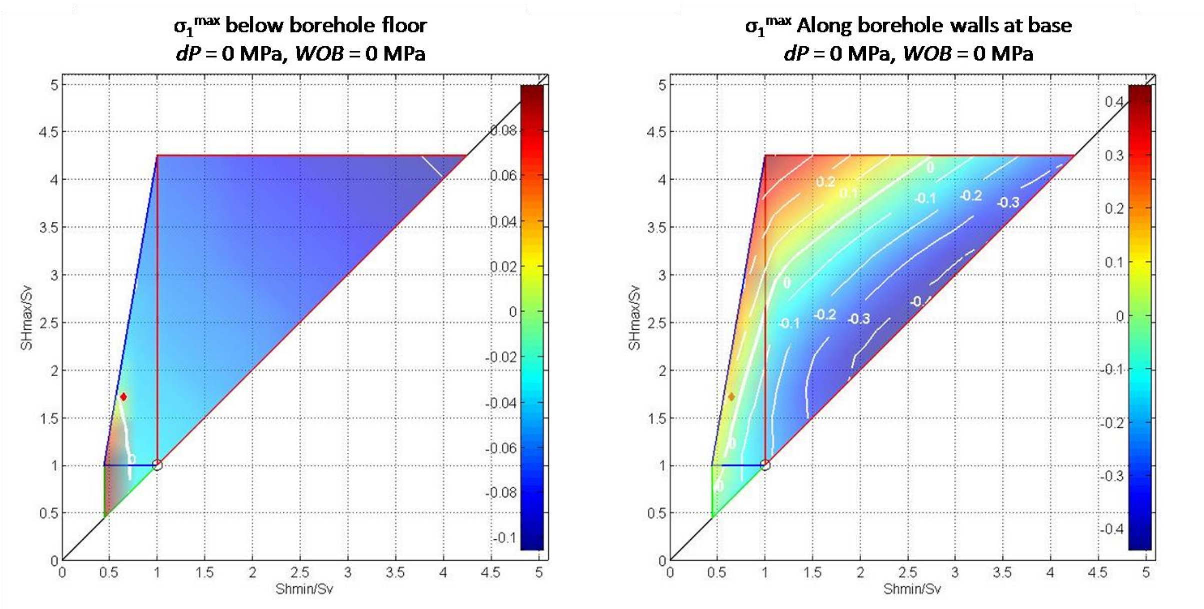

Figure 22. Contoured σ_1^{max} on frictionally limited stress polygon showing (a) the maximum stress below the borehole floor as a function of stress state, and (b) the maximum stress along the lower section of the borehole wall. Boundary conditions dP=0 MPa and WOB=0 MPa. well 58A-10 represented with a red diamond. As before, the thick contour line separates regions of tension from compression and thus the conditions for petal-centerline fracture nucleation.

Tractions consistent with conditions in well 58A-10 act outward from the borehole with WOB strictly applied to the borehole floor and *dP* applied to all borehole surfaces. Figure 23 shows the maximum stress concentration near the borehole floor with local boundary conditions *dP* = 2.48 MPa and *WOB* = 0 MPa. The left side of Figure 23 shows σ_1^{max} below the borehole floor revealing a slight increase in the magnitude of tension if compared to the corresponding left side of Figure 22 with the most notable difference in the normal faulting region. Similarly, the right side of Figure 23 shows a slightly increased region of tensile σ_1^{max} if compared to the case with no excess pressure. This is consistent with increased hoop stress due to this normal traction as predicted by the Kirsch solution and also seen in Figure 11. In Figure 24 the effect of *WOB* is explored with local boundary conditions of *dP* = 0 MPa and *WOB*= 5.16 MPa. Implementation of *WOB* results in a slight increase in the tension of σ_1^{max} below the borehole floor slightly increases tension along the adjacent walls primarily along the corners of the borehole relative to Figure 22.

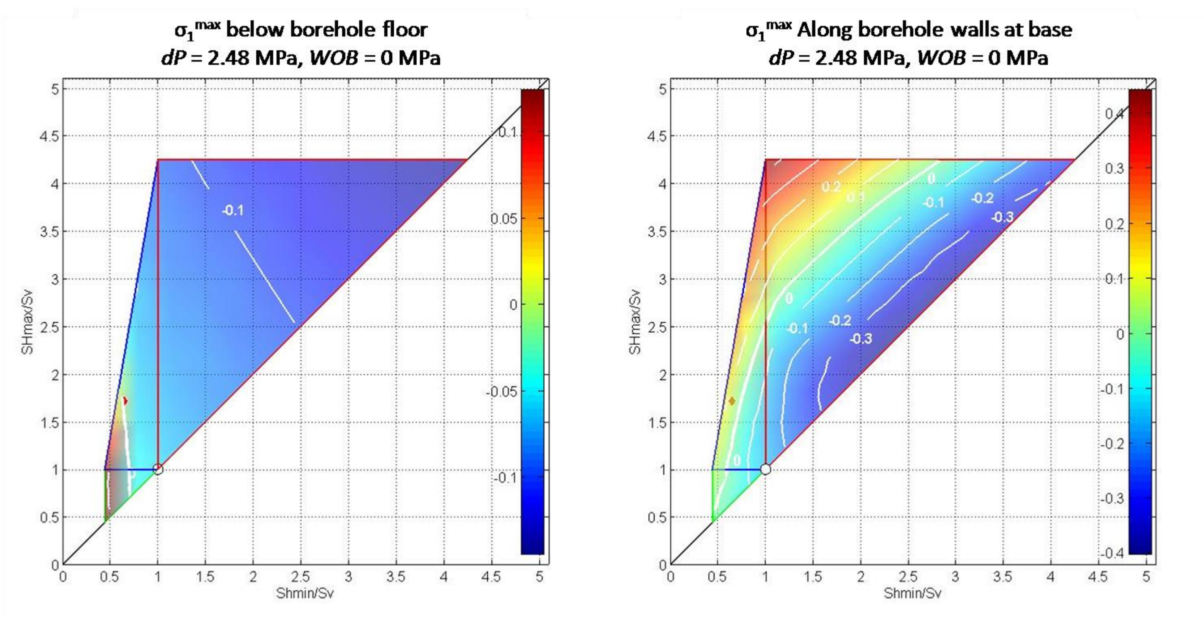

Figure 23. Contoured σ_1^{max} on frictionally limited stress polygon showing (a) the maximum stress below the borehole floor, and (b) the maximum stress along the lower section of the borehole wall. Boundary conditions dP = 2.48 MPa and WOB=0 MPa. Well 58A-10 represented with a red diamond.

Figure 25 maps the results from local boundary conditions *dP* = 2.48 MPa and *WOB* = 5.16 MPa, consistent with conditions in borehole 58A-10. On the left side of Figure 25, borehole 58A-10 lies along the boundary of the region where tensile stresses occur below the borehole floor suggesting that the necessary conditions for nucleation of petal-centerline fractures in this borehole (Davatzes and Hickman, in press) should be highly sensitive to local conditions. Since this borehole lies along the transition, the certainty of tension below the borehole is somewhat ambiguous. Given the abundant occurrence and extensive intervals of petal-centerline fractures in 58A-10 (Davatzes and Hickman, in press) and their apparent occurrence in other wells (personal communication Dr. Judith Sheridan, 2009/11) this result is somewhat surprising. It is important to consider two constraints here: (1) these models should produce minimum estimates of induced tension; (2) this series of models represents a vertical borehole.

However this analysis is confined to vertical wells, and although near vertical, deviation of the 58A-10 borehole reaches up to 12° over a range of deviation direction azimuths. Other boreholes in the field are much more highly deviated. This insight suggests that borehole orientation must be carefully considered.

Tension as indicated by the $\sigma_1^{max} = 0$ contour line spans all three different faulting regimes as in previous cases. However, this combination of boundary conditions expands the region of tension in Figure 25 near the walls above the borehole floor relative to all previous cases reflecting the combined effects of *dP* and *WOB*, and indicating tensile fractures could form. This situation has important implications because the increased complexity of the stress state at this location violates many assumptions made when interpreting classic borehole tensile fractures. Note that the restriction of tension below the borehole floor to approximately 5% of the permissible stress states suggests that the occurrence of petal-centerline fractures can be used to constrain principal stress magnitudes and determine faulting regime.

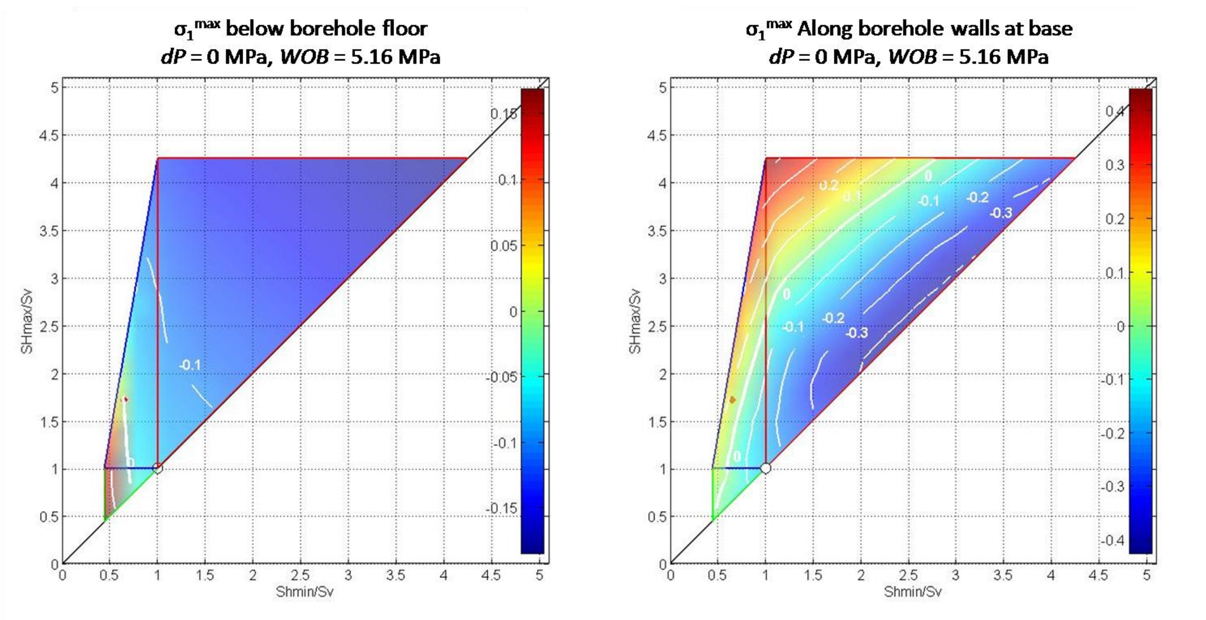

Figure 24. Contoured σ_1^{max} on frictionally limited stress polygon showing (a) the maximum stress bellow the borehole floor, and (b) the maximum stress along the lower section of the borehole wall. Boundary conditions dP = 0 MPa and WOB = 5.16 MPa. Well 58A-10 represented with a red diamond.

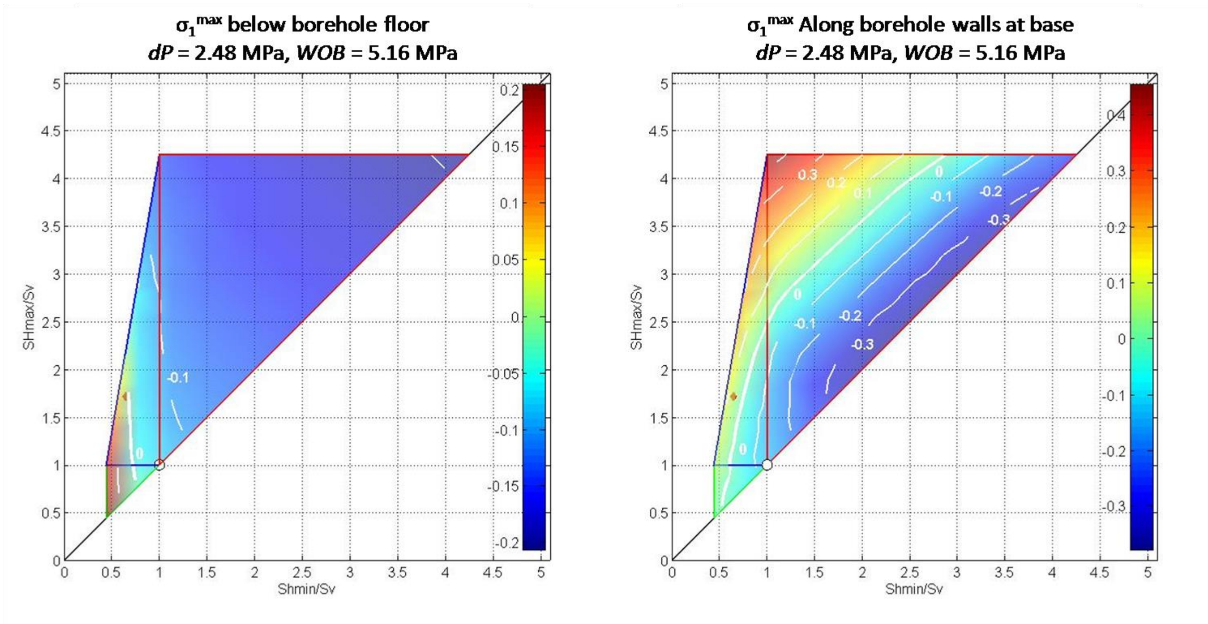

Figure 25. Contoured σ_1^{max} on frictionally limited stress polygon showing (a) the maximum stress below the borehole floor, and (b) the maximum stress along the lower section of the borehole wall. Boundary conditions dP = 2.48 MPa and WOB = 5.16 MPa. Well 58A-10 represented with a red diamond.

3.4 Impact of borehole orientation on stress concentration on its walls and floor

3.4.1 **Methods**

Analysis thus far has adhered to the simplifying assumption of a vertical borehole in which one principal stress, the vertical principal stress, is aligned with the borehole axis. In a general sense, directional drilling, drilling in regions of high topographic relief, or drilling in the vicinity of a large, seismically active fault all imply that one of the principal stresses need not be aligned with the borehole axis. The 2D plane strain solution for the local concentration of stresses on an arbitrarily inclined borehole wall has been solved analytically (Peska & Zoback, 1995) to generalize the original Kirsch solution (please note that appropriate corrections to sign errors in their equations are provided in (Zoback M. D., 2007) and poor documentation of rotation angle definitions are resolved here). The extension of this analysis to the stress state in the vicinity of the borehole floor is the subject of this section.

In this analysis, the local stress state in the vicinity of the wellbore floor is numerically calculated for a series of well deviation angles from vertical and deviation directions. Here, the deviation direction is defined as the azimuth of the borehole measured from north on a horizontal plane; the deviation is the angle measured from vertical down to the borehole in a vertical plane. Therefore a vertical borehole would have a deviation of 0°, while a horizontal borehole would have a deviation of 90°. A borehole with a deviation direction of 0° would point north while one with a deviation direction of 90° would point east.

The aim of this analysis is to characterize the stress state below the borehole floor as a function of deviation and deviation direction. To simplify the analysis and facilitate comparison with previous results, the set of simulations continue to use the stress state associated with the 58A-10 borehole (Table 3). In addition, to aid in automating the large set of simulations, the well mesh remained fixed and instead the stress tensor was rotated via tensor transformation to correspond to the effect of the well deviation and deviation direction. According to the tensor transformation rule, the stress components σ_{ij} of an initial system can be transformed into the components σ'_{ij} in a rotated system as follows:

$$\sigma'_{ij} = A\, \sigma_{ij} A^T \qquad (8)$$

where A is the rotation matrix and A^T its transpose. The tensor transformation of the initial stress state into the inclined stress state by the deviation and deviation direction was performed in two successive two-dimensional rotations: (1) A rotation equivalent to the deviation direction angle was accomplished by performing a rotation of the initial stress state around the z-axis by an angle beta β, in which a new reference frame we may call *x',y',z* was defined. The stress tensor transformation was computed as follows:

$$\sigma'_{dev\,dir} = \begin{bmatrix} \cos\beta & \sin\beta & 0 \\ -\sin\beta & \cos\beta & 0 \\ 0 & 0 & 1 \end{bmatrix} \sigma \begin{bmatrix} \cos\beta & -\sin\beta & 0 \\ \sin\beta & \cos\beta & 0 \\ 0 & 0 & 1 \end{bmatrix} \qquad (9)$$

(2) A rotation equivalent to the deviation angle of the well was accomplished by performing a rotation on the previously rotated stress tensor ($\sigma'_{dev\,dir}$) around the x'-axis by an angle delta δ, in which a new reference frame *x', y'', z'* was defined. The final stress tensor transformation was computed as follows:

$$\sigma'_{final} = \begin{bmatrix} 1 & 0 & 0 \\ 0 & \cos\delta & \sin\delta \\ 0 & -\sin\delta & \cos\delta \end{bmatrix} \sigma'_{dev\,dir} \begin{bmatrix} 1 & 0 & 0 \\ 0 & \cos\delta & -\sin\delta \\ 0 & \sin\delta & \cos\delta \end{bmatrix} \qquad (10)$$

To avoid confusion it is important to note that both rotation angles (β and δ) are in the opposite sense of those from the deviation and deviation direction of the well since we treat the well as fixed and the stress state as rotating. In other words, a clockwise rotation of the well in a fixed stress state would be proportional to a counterclockwise rotation of the stress state in a fixed vertical well. Figure 26 shows a cartoon representation of the tensor transformation performed, the rotation by deviation direction and deviation are shown in (b) and (c) respectively.

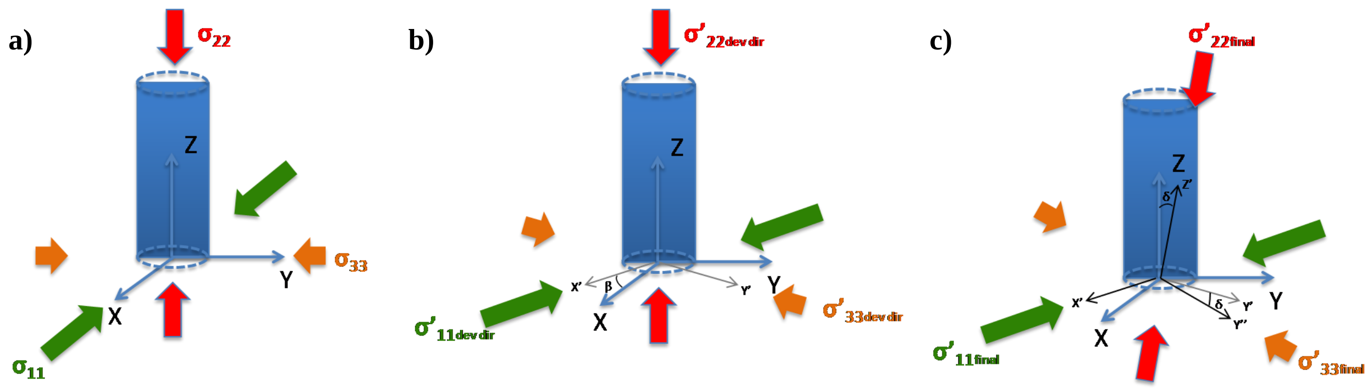

Figure 26. Stress tensor transformation. (a) Initial stress state. (b) Rotation equivalent to the deviation direction, new reference frame x',y',z. (c) Rotation equivalent to the well deviation, new reference frame x',y'',z'.

The mesh defining the borehole and observation grid developed in previous sections were used to model the effect of the deviation and deviation direction on σ_1^{max} occurring below its floor and along the adjacent borehole walls. A total of 91 stress rotations were performed to represent the 91 well directions marked by blue circles in Figure 31; equivalent to rotating through deviation directions from 000 to 090 and deviations from 0° to 90° each spaced at 10° degree increments. Because of the symmetry of the problem, this should adequately represent a full range of well orientations. As before, results of these analyses are contoured to map the dependence of σ_1^{max} on well orientation.

3.4.2 **Results**

The contours of the local σ_1^{max} magnitude in the vicinity of borehole floor for a selection of deviations in the S_{Hmax} and S_{hmin} deviation directions, and subjected to all local borehole boundary conditions consistent with the 58A-10 borehole, are shown in Figure 27 and Figure 28, respectively. The left column shows the deviation for which the resolved stresses were numerically calculated. The middle and right columns show the most tensile local principal stresses resolved in the S_v-S_{hmin} plane and the S_v-S_{Hmax} plane respectively. In each case, a hollow black diamond shows the projection onto the plotted surfaces of the σ_1^{max} (most tensile stress found in the simulation) located below the borehole floor, similarly a hollow circle maps the location of the σ_1^{max} above the borehole wall and along the walls. Since all computations are made farther than one mesh element away from the well, the tensile stress computed is underestimated and therefore represents a conservative prediction of tension and related potential for the nucleation of petal-centerline fractures. As above, a thick white line corresponds to $\sigma_1^{max} = 0$, defining the boundary between tension and compression.

The first case (deviation 0°) shows the stress around a vertical well, on the S_v-S_{hmin} plane, two characteristic stress concentration lobes appear in the failure plane front; while the S_v-S_{Hmax} plane shows the larger magnitudes of σ_1 to be located below the floor. The maximum tensile stress magnitude (hollow black diamond) was computed to be 0.064 MPa; which indicates that the nucleation of petal centerline fractures is feasible under the modeled conditions for a vertical well. The maximum σ_1^{max} magnitude below the borehole floor for all deviations and deviation directions modeled are summarized in Table 5.

Table 5.Summary of selected maximum most tensile principal stress, σ_1^{max}, in the vicinity of the borehole floor.

Deviation	Deviation direction	Maximum S_1 [MPa]
0°	0	0.064
20°	S_{Hmax}	4.09
50°	S_{Hmax}	13.87
90°	S_{Hmax}	9.99
20°	S_{hmin}	-9.30
50°	S_{hmin}	-6.44
90°	S_{hmin}	-8.10

As the borehole deviation in the S_{hmax} direction increases from 0° to 90°, the maximum concentration of tensile stress below the floor reaches its highest magnitude at a deviation of approximately 50°. Note that the two stress concentration lobes migrate to the S_v-S_{Hmax} plane as soon as the well is deviated in the S_{Hmax} direction. In general, σ_1^{max} near the borehole floor tends to get amplified on both observation planes when deviated in the S_{Hmax} direction. Contrastingly, tension was never generated below the floor of the boreholes deviated along the S_{hmin} direction. However, for the same inclinations, tensile stresses developed on the walls of the borehole and are shown in the S_v-S_{Hmax} plane.

Figure 29 shows the concentration of stresses on a plane below the borehole floor and orthogonal to the borehole axis, corresponding to the same combinations of deviation and deviation direction illustrated in Figure 27 and Figure 28. For a vertical well, the maximum concentration of stress occurs near the periphery of the borehole floor, towards the S_{hmin} direction. As the well is deviated along the S_{Hmax} direction, the tensile region migrates towards the side of the borehole bottom that is higher and tends to align with S_{Hmax}. Tickmarks represent the direction of σ_1. Thus, if a petal-centerline fracture is to initiate it would most likely propagate in the direction perpendicular to the tickmark. Again, no concentration of tension was present in boreholes deviated along the S_{hmin} direction.

Deviation   Deviation Direction: East – S_{Hmax} direction

0°

20°

50°

90°

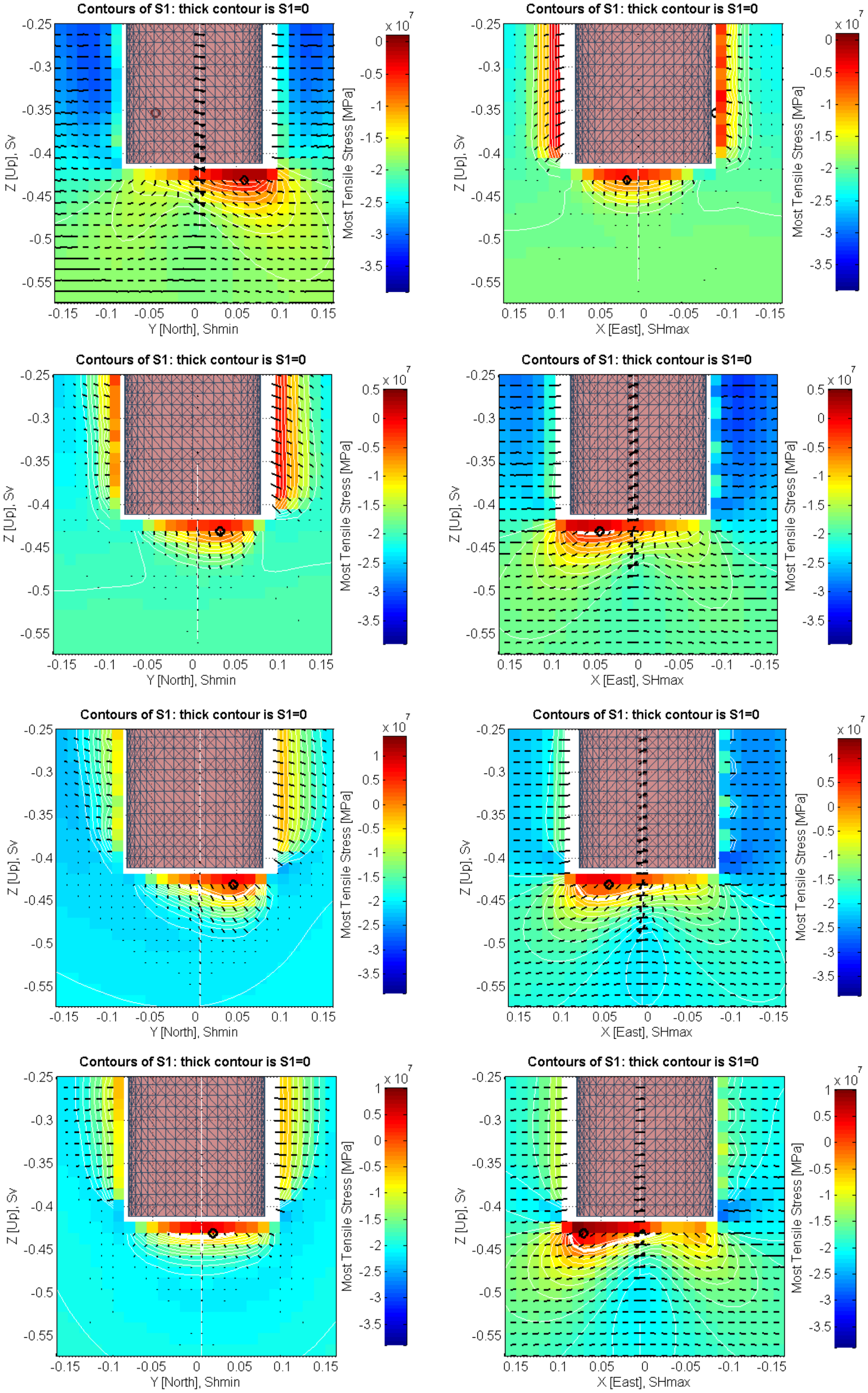

Figure 27. Impact of deviation along the S_{Hmax} direction for deviations of 0°, 20°, 50° and 90°.

Deviation **Deviation Direction : North – S_{hmin} direction**

20°

50°

90°

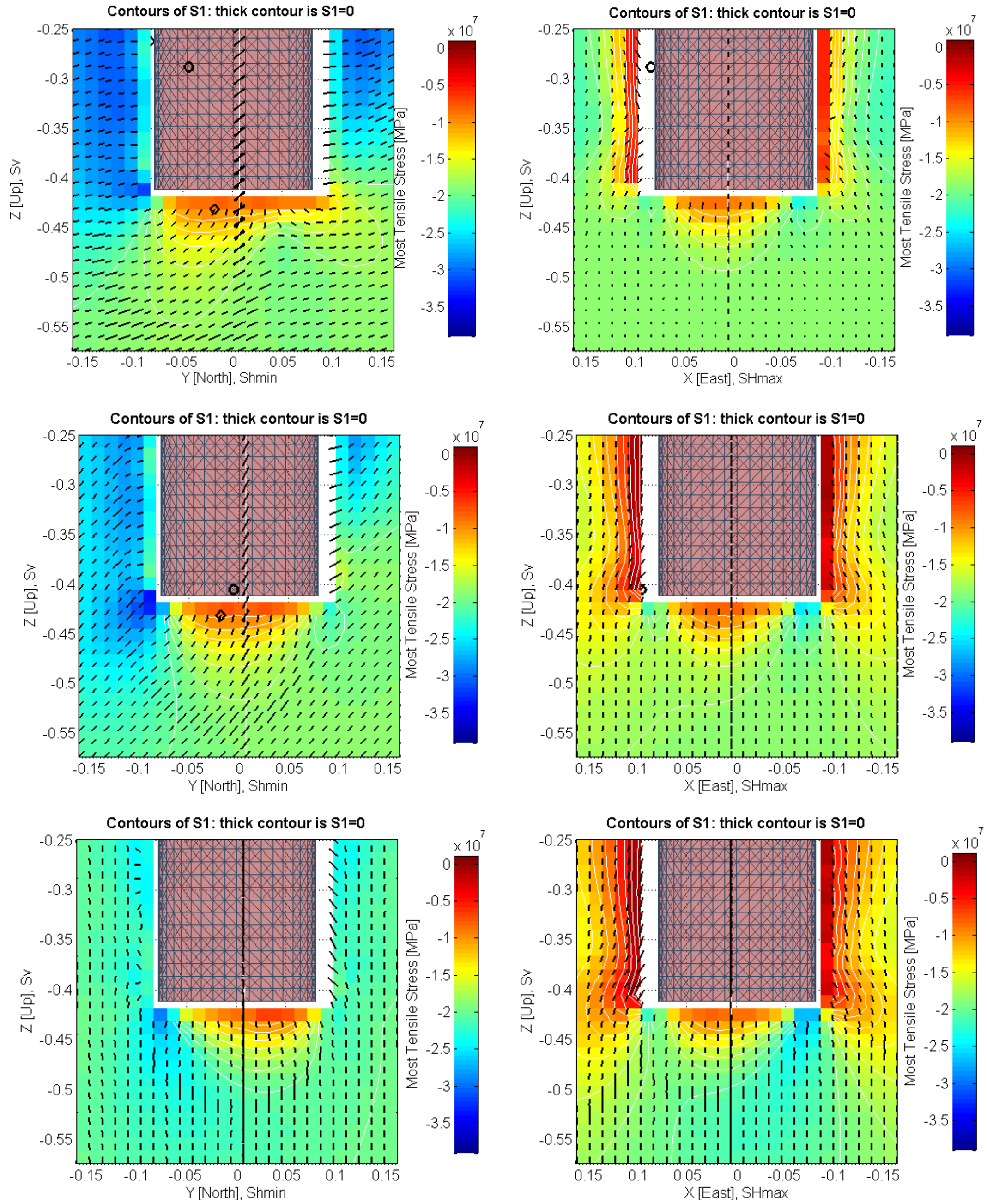

Figure 28. Impact of deviation along the S_{hmin} direction for deviations of 20°, 50° and 90°.

Deviation **S_{Hmax} Deviation Direction** **S_{hmin} Deviation Direction**

0°

20°

50°

90°

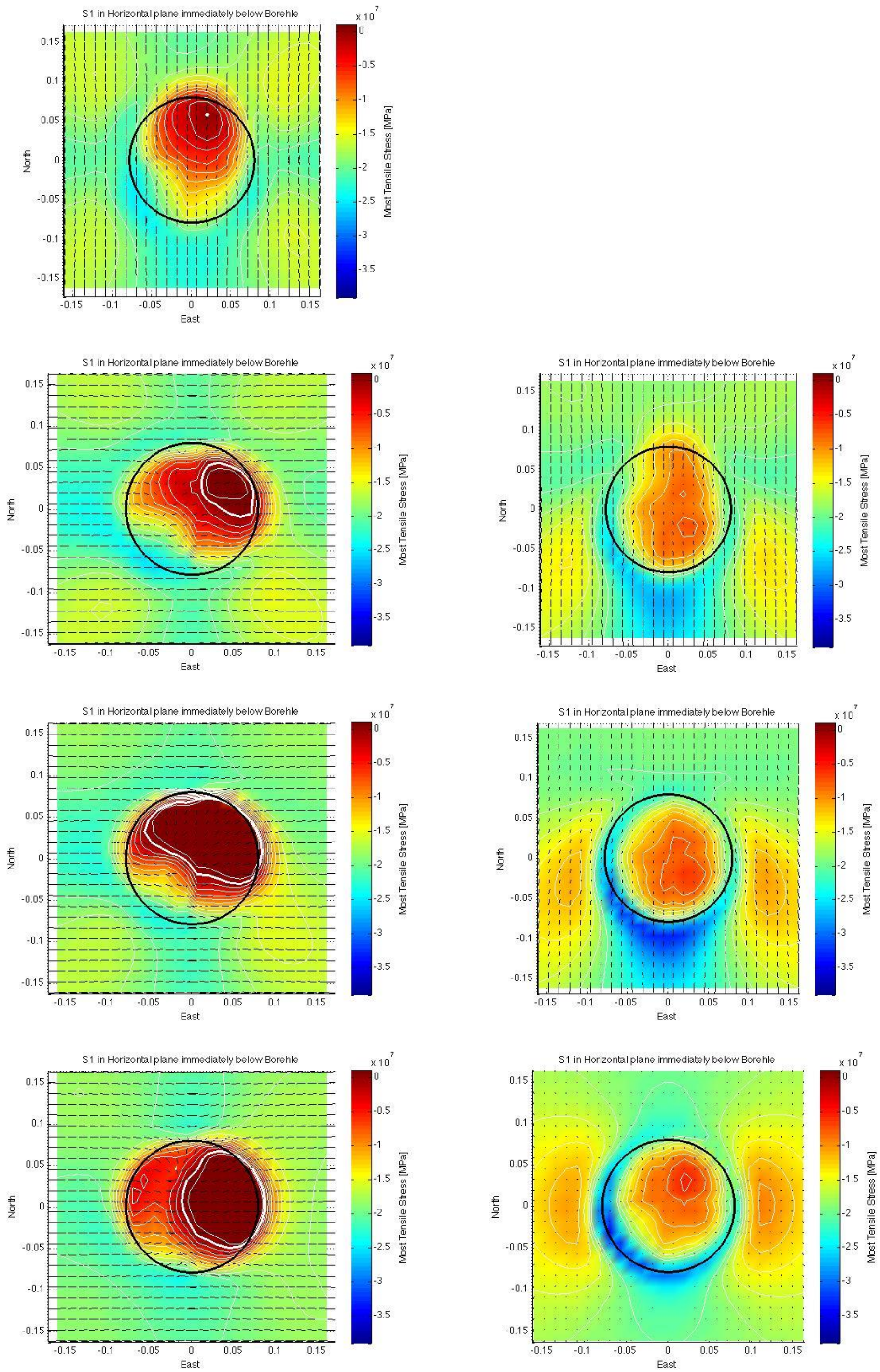

Figure 29. Concentration of stress below the inclined boreholes on a plane parallel to the floor. The central column show boreholes deviated along the S_{Hmax} direction, while the right column shows the boreholes deviated along the S_{hmin} direction. As in Figure 27 and Figure 28, S_{hmin} is oriented N-S.

A lower hemisphere, equal area stereographic projection, also known as a stereogram, is employed to visualize the maximum concentration of stresses on a well as a function of its deviation and deviation direction. A stereogram is a projection of a lower hemisphere on a horizontal plane; the equal area designation indicates it attempts to preserve line length when projecting the inherently 3D hemisphere into a 2D grid. In this projection, a vertical well is represented as a point in the center, while a horizontal well would be a point lying on the stereogram's periphery. Thus the magnitude of σ_1^{max} at any position on the stereogram corresponds to the simulations deviation and deviation direction. For reference, red arrows indicating the direction of the remote principal stresses are provided such that the minimum remote stress S_{hmin} is oriented along the North-South direction; however, the corresponding stress in the Coso Geothermal Field is oriented along an azimuth of 108° ± 15°. This step aids in analyzing the dependence of the local stress state on borehole orientation and the discrepancy can be resolved by simple rotation of –108 about a vertical axis.

For reference, the Kirsch solution was first mapped onto a stereogram to visualize the maximum stress concentrated on the borehole walls. Figure 30 shows the maximum concentration of local principal stress σ_1^{max} on the walls of a borehole (and far away from its floor) subjected to the stress state from well 58A-10 (Table 3) for any possible inclination (for derivation see Peska & Zoback, 1995, and Zoback, 2007). Note that for the given remote stress state, the concentration of tensile stresses on the wall is maximized as the deviation of the well approaches verticality, corresponding to the orientation of the well in which differential stress across the well walls is maximized. The tensile region extends farther for deviation directions aligned towards the S_{hmin} direction. This figure illustrates the possible combinations of deviation and deviation direction for which a tensile fracture would appear on a borehole wall subjected to the strike-slip stress state of well 58A-10.

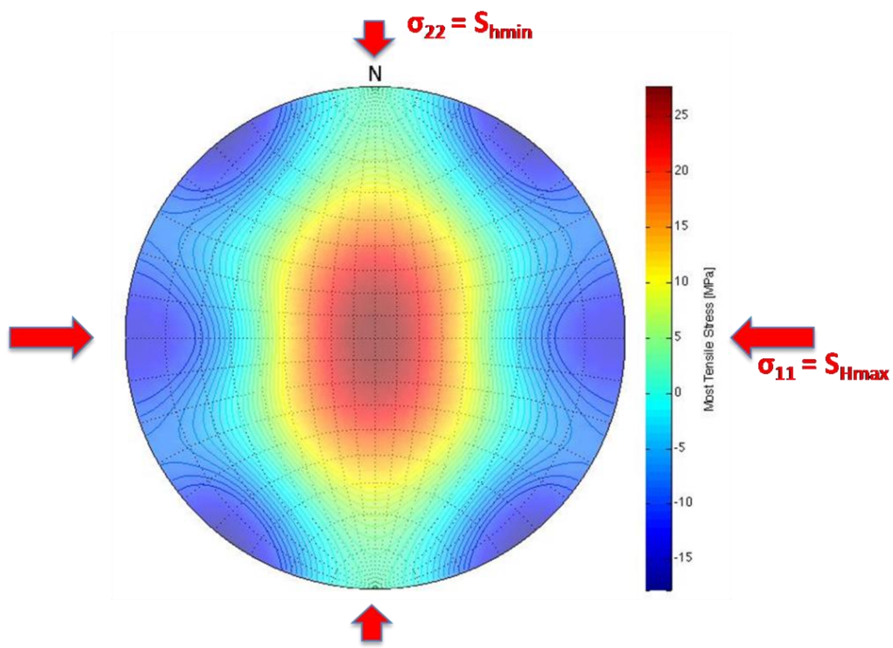

Figure 30. Stereogram mapping the maximum concentration of local principal stress σ_1^{max} on the walls of a wellbore as a function of all possible combinations of deviation and deviation direction.

In contrast to the simple case described by Peska and Zoback (1995) and illustrated in Figure 30, Figure 31 shows the maximum concentration of stress around the borehole floor for the stress state acting on well 58A-10 and boundary conditions of zero weight on bit and no excess pressure. The resulting variation in σ_1^{max} magnitude below (Figure 31, left) and along the nearby borehole walls (Figure 31, right) resulting from arbitrarily inclined, flat-bottomed borehole is clearly non-intuitive. Note that a wide range of inclinations are associated with tension below the borehole floor, which is assumed to be indicative of the nucleation of petal-centerline fractures. The higher concentration of tensile stresses are clustered in two symmetrical regions spanning about 80° and distributed along the S_{Hmax} direction.

Figure 31 (right) maps σ_1^{max} along the borehole wall within 4 radii of the borehole floor. Note that the concentration of tensile stresses do not conform with the solution presented in Figure 30 for the concentration of stresses on the walls developed by Peska & Zoback. This discrepancy reflects the influence the wellbore floor has on the concentration of stresses in its vicinity.

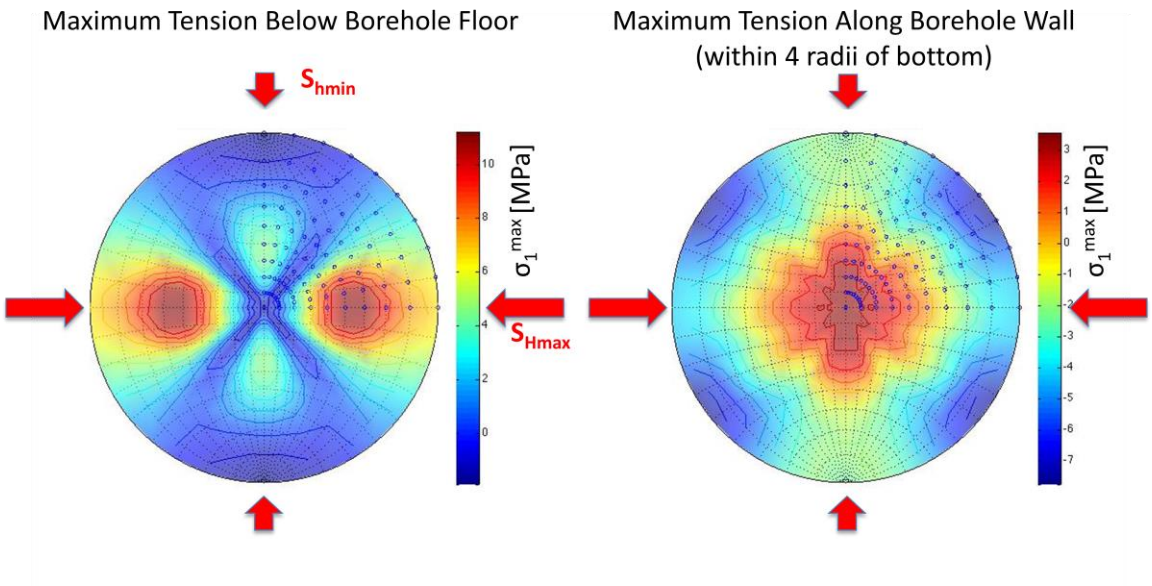

Figure 31. Stereogram mapping σ_1^{max} below the borehole floor (a), and along the wall near the bottom (b), for all possible well inclinations. The stress state is that of well 58A-10. Boundary conditions: dP = 0 MPa, WOB = 0 MPa. Simulated borehole orientations are indicated by blue dots. In this and subsequent figures, all contours are plotted at a 1 MPa interval.

The impact of borehole boundary conditions including *dP* and *WOB* on the magnitude of σ_1^{max}, were systematically investigated duplicating the approach used in Section 3.3. Figure 32 shows σ_1^{max} in the case where *WOB* = 0 MPa and *dP* = 2.48 MPa. Note that the excess pressure is the only parameter that changed from the previous case (Figure 31). This excess mud pressure caused a decrease in the range of well inclinations where concentrations of tension below the borehole floor occur. In this scenario, tensile stresses occur in deviations higher than 10° along the direction of S_{Hmax} and the maximum tension magnitude has increased as compared with Figure 31. In contrast, the range of inclinations for which σ_1^{max} is tensile along the borehole wall near the floor increased, as revealed on the right side of Figure 32.

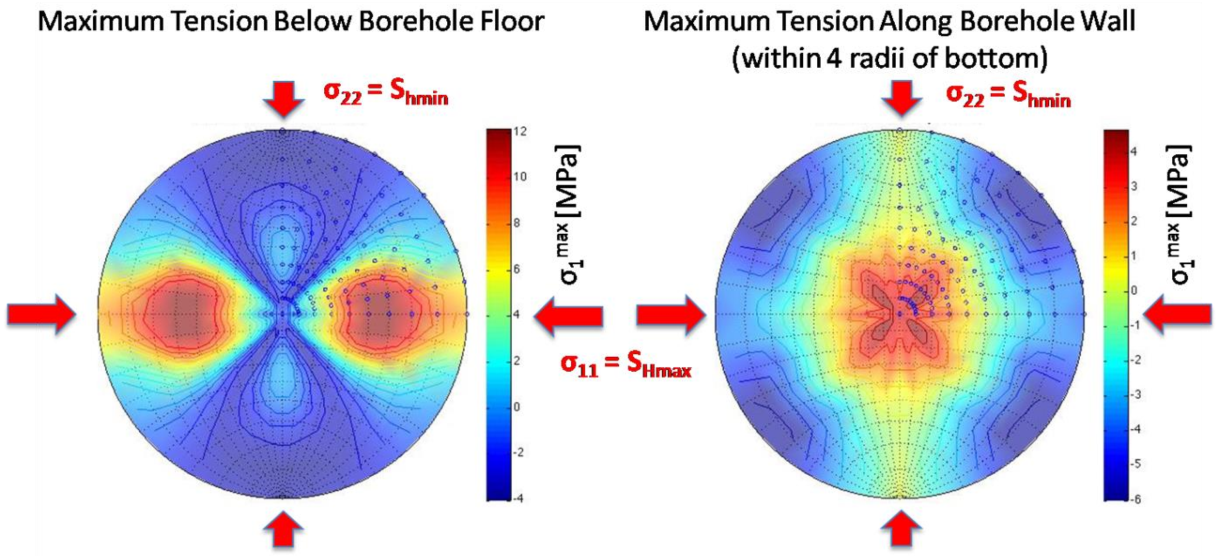

Figure 32. Stereogram mapping σ_1^{max} below the borehole floor (a), and along the wall near the bottom (b), for all possible well inclinations. The stress state is that of well 58A-10. Boundary conditions dP=2.48 MPa and WOB = 0 MPa. Color bar in MPa.

The impact of the *WOB* on σ_1^{max}, is illustrated in Figure 33 with local borehole boundary conditions of *dP* = 0 MPa and *WOB* = 5.16 MPa. This analysis of σ_1^{max} in the vicinity of the borehole floor severely reduced the range of deviations where tension occurs in the direction of S_{hmin}, while the tensile region distributed along the S_{Hmax} direction increased compared to Figure 31 to a 90° span. Figure 32 and Figure 33 reveal that whereas the applied *dP* still allows the formation of tension along the S_{hmin} direction, the applied *WOB* completely restricts it. However, the *WOB* causes greater tensile stresses below boreholes oriented at any inclination along and ± 30°from the direction of S_{Hmax}. The right side of Figure 33 reveals that *WOB* reduces the range of deviations along the S_{hmin} direction where tensile fractures could occur by approximately one third compared to the case with *dP* (right side of Figure 32).

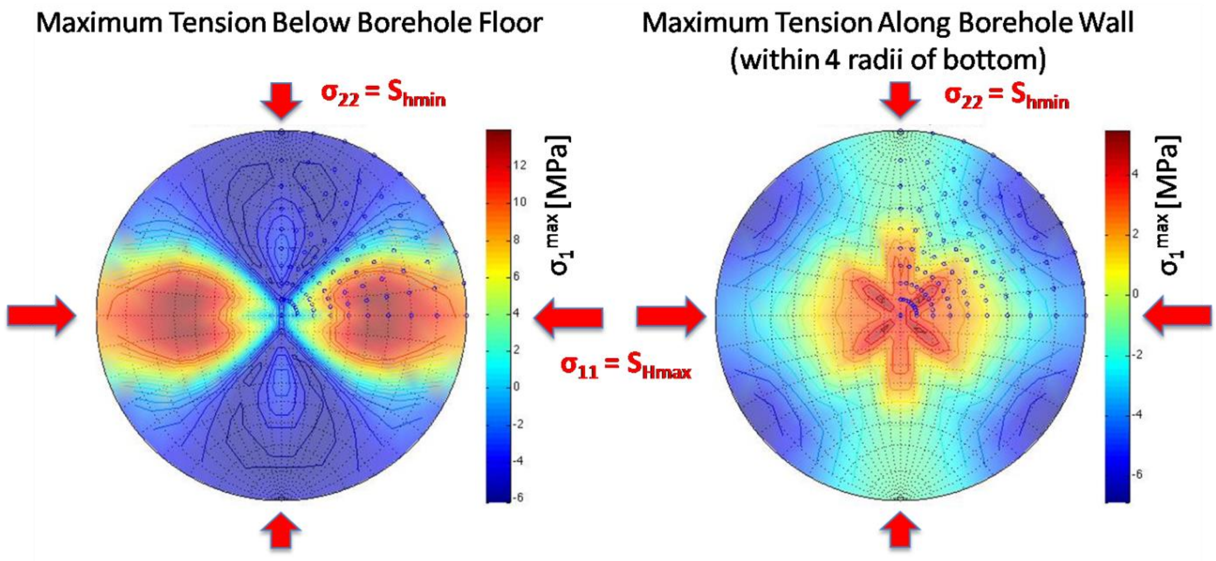

Figure 33. Stereogram mapping σ_1^{max} below the borehole floor (a), and along the wall near the bottom (b), for all possible well inclinations. The stress state is that of well 58A-10. Boundary conditions dP=0 MPa and WOB = 5.16 MPa. Color bar in MPa.

Both *WOB* and *dP* are implemented in Figure 34, essentially revealing the propensity for tension below the borehole floor for any borehole orientation in the vicinity of the 58A-10 borehole. This case essentially superposes effects illustrated in the previous two cases. This case indicates that the region where tensile stress occurs below the borehole floor is exclusive of deviation directions spanning approximately 100° along the S_{Hmax} direction; therefore, as predicted by Figure 28, σ_1^{max} never becomes tensile for deviations along the S_{hmin} direction. Note also that the magnitude of the tensile stresses in some inclinations reach up to 15 MPa. The right side of Figure 34 suggests that tensile fractures could appear on the borehole walls under the modeled conditions for any deviation along the S_{hmin} direction; however, only deviations between 0° to 50° would generate tension along the S_{Hmax} direction. It is important to note that deviation has a significant impact on the magnitude of σ_1^{max} especially below the borehole floor, suggesting that even small deviations would significantly change the shape of the tensile region in contours of σ_1^{max} in frictionally limited stress polygons as those shown in Figure 25.

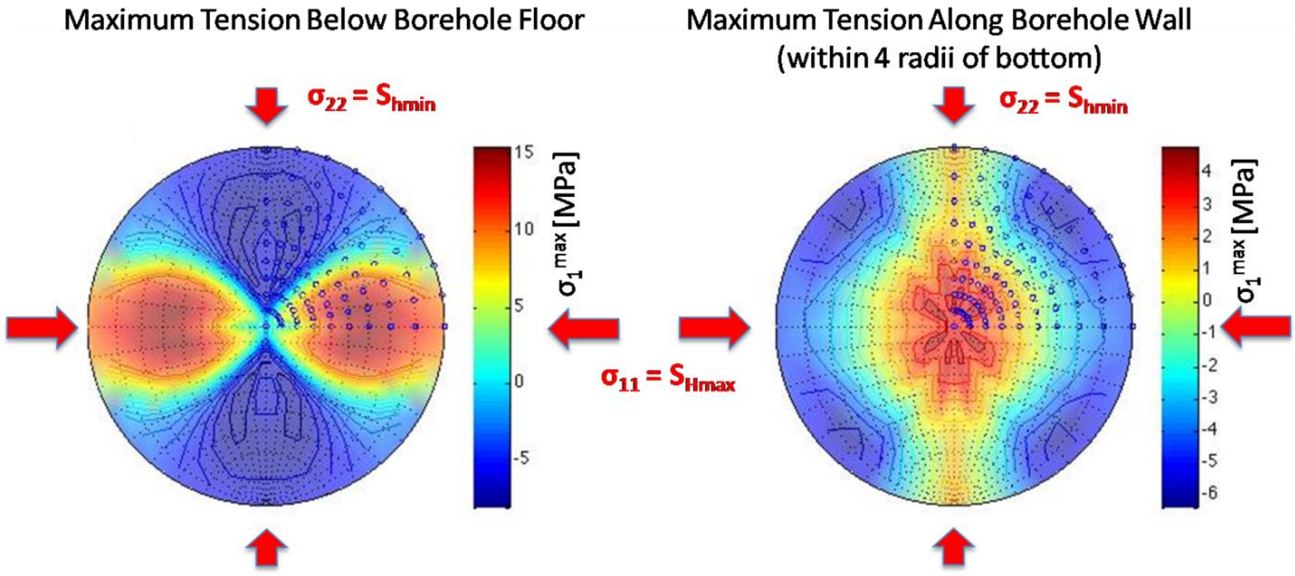

Figure 34. Stereogram mapping σ_1^{max} below the borehole floor (a), and along the wall near the bottom (b), for all possible well inclinations. The stress state is that of well 58A-10. Boundary conditions dP=2.48 MPa and WOB = 5.16 MPa. Color bar in MPa.

In the Coso Geothermal Field, S_{hmin} is oriented along an azimuth of 108° ± 15°. Well 58A-10 has a deviation from vertical of 4.2° and a deviation direction of 331° from North. At such inclination conditions the stereogram in Figure 34a shows a concentration of tension below the borehole floor of approximately 4 MPa. Such concentration of stress predicts the nucleation of petal-centerline fractures, which is consistent with the physical observation of such features in well 58A-10 at the stress state and boundary conditions modeled.

4 DISCUSSION

The way stresses are resolved on a borehole floor subjected to remote principal stresses is non-intuitive and there is no analytical solution that describes it. Prior to this study, the most detailed published work investigating the stress state in the vicinity of a borehole floor and the nucleation of petal-centerline fractures was conducted by Li & Schmitt (1997). At that time, petal-centerline fractures were recgonized in core, but not yet in image logs of wells. They investigated the sensitivity of the stress state below the floor of a vertical borehole for floor geometries associated with coring. In their analysis, they subjected this borehole floor geometry to a limited range of stress states using the finte element method and demonstrated that tension below the borehole is promoted at the corner and extends from the curf of the coring bit and as the core stub length extends. This geometry and resulting evolution of the stress state is substantially different from the borehole studied here. In addition, these studies did not addresss the impact of borehole orientation or provide the resolution across realistic remote stress boundary conditions developed here due to computational limitations. It is also important to note, that this study provides a benchmark against a known well containing petal-centerline fractures with well constrained stress state, which has previously been lacking.

Several critical opportunities result from the extension of the previous work presented in this study. In particular, the analysis of petal centerline fracture occurrence potentially provides an additional method to investigate the remote principal stress state in the rock volume penetrated by a borehole. Currently, reliable methods for estimating actual in situ principal stress magnitudes at great depth are limited to methods including mini-hydraulic fracturing experiments that measure the least compressive principal stress, integration of overburden weight to estimate the vertical stress, and analysis of breakout width to constrain the remaining principal stress magnitude (see reviews in Zoback et al., 2003; Zoback, 2007; Jaeger et al., 2007). Orientation and relative principal stress magnitudes can also be inferred from borehole deformation (tensile fractures and breakouts) and focal mechanism inversion. Typcially all of these methods must be combined to estimate the three dimensionl stress state (e.g., Davatzes and Hickman, 2006; 2007). However, it is much more typical for one of these critical data sets to be missing and thus an additional method could provide a significant improvement. In particular, breakout formation is favored in high differential stress reverse faulting environments and generally absent in normal faulting environments. To determine if this is a viable method, it is necessary to understand the relationship of petal-centerline fractures to the key boundary conditions including material properties, tractions resolved on the borehole surface, and remote stresses, and the borehole geometry and orientation.

- **Material properties and local boundary conditions**

The sensitivity of generating tensile stress below a vertical borehole to common material properties and boundary conditions on the borehole wall is a key concern for potential to use petal centerline fractures to estimate the remote principal stress magnitudes or directions. To investigate this issue, material properties including Poisson's ratio and traction boundary conditions including *dP* and *WOB* for reasonable ranges of these parameters were simulated in the stress state from Coso well 58A-10. Generation of tension below the borehole floor proved to be insensitive to Poisson's ratio, although it has a significant impact on the stress along the adjacent borehole walls within the region of influence. A substantial impact is detected on both locations for differential mud pressure in excess of formation fluid pressure such that an increase in the absolute magnitude (positive or negative) promotes tension mud pressure. However, for small magnitudes from -1MPa to 5 MPa, tension below the borehole floor is inhibited for the modeled vertical borehole orientation and stress state pertinent to Coso borehole 58A-10. *WOB* demonstrates a similar, albeit less significant effect.

- **Dependence of Tension below the Borehole Floor on Stress state**

A systematic study of the stress perturbation below a borehole as well as on the parameters impacting such distribution has been accomplished. The local stress field near a borehole subjected to a series of stress states permissible in the frictionally limited shallow Earth crust reveals unique characteristics in comparison to the results from the Kirsch solution. The proximity of the borehole floor favors the generation of tension on the adjacent walls over a wider range of stress states not present in the Kirsch solution. This is illustrated by a significant curvature of the transition from tension to compression in the stress polygon contour of the σ_1^{max} developed on the walls near the floor. The tensile region in the contoured stress polygons was revealed to extend into a much larger proportion of the reverse faulting regime and into the normal faulting regime, although still minimizing mean stress and maximizing horizontal differential stress. Tension revealed in maps of σ_1^{max} variation due to stress state indicate the potential for tensile fractures to form along walls where the stress state is strongly perturbed by the borehole floor. If tensile fractures form in this location their relationship to the remote principal stress is compromised. In many intervals of well 58A-10 (personal communication, Nick Davatzes 2010/01/27) features similar to tensile fractures are visible in image logs occurring in four symmetric quadrants, while in other regions the features curve. This potential ambiguity which requires these intervals to be excluded from interpretation might be explained by early formation of tensile fractures in the borehole wall but near the borehole floor. Only a very small fraction of the stress polygon corresponding to low mean stress is associated with tension under the borehole floor; therefore, revealing that in vertical boreholes petal-centerline fractures would only take place in normal to strike-slip faulting regimes

- **Dependence of Tension below the Borehole Floor on Borehole Orientation in the Stress Field**

The concentration of tension below a borehole floor under the stress state and boundary conditions studied proved to be highly sensitive to the borehole deviation and deviation direction. A high σ_1^{max} gradient centered along the S_{Hmax} direction combined with the lack of tension under the remaining deviations reveal that the occurrence of petal-centerline fractures on an inclined borehole would indicate a deviation within ±50° from the S_{Hmax} principal direction. The increase in tension along such deviations may imply a wider range of stress states under which a petal-centerline fracture would occur when the borehole is inclined. The stereogram mapping the σ_1^{max} developed on the walls near the floor of an arbitrarily inclined borehole reveals a similar contour to that predicted from the Kirsch solution. Implying that the borehole proximity has a minor impact on the range of inclinations under which tension occurs along the walls.

- **Estimates of Remote Principal Stresses from occurrence of Petal-Centerline Fractures**

For a vertical well, the range of stress states in which petal-centerline fractures can nucleate is highly restricted (Figure 25). This suggests that the occurrence of these structures provides important insight into the stress state in the vicinity of a borehole. In addition, the occurrence of tension is highly sensitive to borehole deviation and deviation direction relative to the remote principal stresses (Figure 34). Small increases in deviations towards S_{Hmax} can significantly increase the magnitude of tension and by implication the range of stress states that can produce petal-centerline fractures. This sensitivity provides a tool for constraining stress magnitude in fields where petal-centerline fractures are detected, but their occurrence correlates to the deviation and deviation direction as it varies along a single borehole or among multiple boreholes within a small region. It is also important to note that although these models are highly sensitive to traction boundary conditions including excess mud pressure and weight on bit, these parameters are generally recorded in mud logs and thus available to constrain the necessary simulations to estimate the remote principal stress magnitudes.

Although not the primary focus of this study, the estimation of remote principal stress direction from borehole deformation is a tool widely used for both academic studies of tectonics, seismic hazards analysis, borehole stability analysis, and stimulation planning in petroleum and geothermal fields. Initial interpretation of these results suggests that tensile fractures can form near the borehole floor and that in this location the attitude of σ_1^{max} might not conform with predictions of the 2D Kirsch solution (Kirsch, 1898; see summary in Zoback, 2003), not even with the 3D generalization (Peska and Zoback, 1995; see summary in Zoback, 2007). Generally, the stress perturbation and resulting potential for tension induced this close to the borehole floor appears to be less than in the 2D case for a vertical well (although further investigation for deviated wells is warranted). This suggests that tensile fractures formed near the borehole floor should be rarer than those formed in the simpler 2D case, limiting the potential for confusion. Furthermore, thermal contraction significantly increases the potential for tension along the borehole wall as it is exposed for long time to circulated borehole fluids, thus further promoting tensile fracture growth (although as discussed it is neglected in this analysis since this situation does not apply to the borehole floor). Nevertheless, significant potential for tension in the stress state at Coso borehole 58A-10 is predicted by simulations in Figures 25 and 34. This result could explain intervals in this well in which 2 sets of features of distinct orientation visible in image logs, and generally fitting the criteria for tensile fractures, occur and render the stress orientation of that interval un-interpretable.

5 CONCLUSIONS

A numerical model was developed using Poly3D to simulate the distribution and magnitude of stress concentration in the vicinity of the borehole floor, and determine the conditions under which petal-centerline fractures nucleate. It has been shown that the observation of petal-centerline fractures can be used as a complementary way to constrict the stress state under which they form.

Since boundary elements do not allow direct observation of the stress resolved at the borehole wall due to the singularities resulting from treating the elements discretizing the borehole surface as dislocations, a model was constructed contrasted by the Kirsch solution to balance the computational load resulting from smaller element size against a calculation of the stress concentration adequate to detect tension. This model was subsequently implemented to analyze the impact the boundary conditions, the remote stress state, and deviation of the borehole have on the way stresses are resolved below the borehole floor.

A systematic study on the parameters that contribute to the concentration of tension below the borehole floor and therefore to the nucleation of Petal-Centerline fractures have been presented for the stress state at Coso well 58A-10. The sensitivity analysis on the boundary conditions showed that the concentration of tension below the borehole floor is not considerably impacted by the Poisson's ratio of the hosting rock. It was also revealed that magnitudes of excess mud pressure close to those of the formation pore pressure ($-1 \geq dP \geq 5$ MPa) restrain the generation of tension below the borehole floor. The same is the case for magnitudes of *WOB* below 8 MPa. However, Poisson's ratio, *dP* and *WOB* they all favor the generation of tension along the borehole walls adjacent to the floor.

The maximum magnitude of σ_1 below the borehole floor was evaluated over the frictionally permissible stress states in the Earth's brittle crust and contoured over a stress polygon, indicating that only a very small fraction of the stress states, corresponding to low mean stress, is associated with tension under the borehole floor. This revealed that in vertical boreholes petal-centerline fractures would only take place in normal to strike-slip faulting regimes. The concentration of tension below a borehole floor under the stress state and boundary conditions studied proved to be highly sensitive to the borehole deviation and deviation direction. The generation of tensile stress below the borehole floor is exclusive of deviation directions spanning approximately 100° along the S_{Hmax} direction. The simulations revealed that while the borehole floor has a strong influence on the generation of tension on the adjacent walls over a wider range of stress states not present in the Kirsch solution, the borehole proximity has a minor impact on the range of inclinations under which tension occurs along the walls.

The simulations have demonstrated that a borehole under the stress boundary conditions present at Coso well 58A-10 is able to amplify the stress concentration to produce tension below the borehole floor; congruent with the observation of petal-centerline fractures in cores and image logs. These results prove that the occurrence of petal-centerline fractures can be used to constrain principal stress magnitudes and determine faulting regime.

This work has accomplished two major outcomes: (1) it has been proved that petal-centerline fractures are suitable to be used as a tool in constricting the remote stress state under which they appear. (2) Tension has been found to appear on the borehole walls near the floor potentially indicating the existence of tensile fractures that may not comply with the assumptions made when they are interpreted.

REFERENCES

Anderson, E. (1951). The Dynamics of Faulting and Dyke Formation with Applications to Britain.

Byerlee, J. D. (1978). Friction of rock. *Pure Appl Geophys , 116*, 615–626.

Crouch, S., & Starfield, A. (1983). *Boundary Element Methods in Solid Mechanics.* Allen and Unwin, London.

Davatzes, N., & Hickman, S. (2007). *Evolution of vertical permeability in Coso Geothermal Well 58A-10.* American Geophysical Union.

Davatzes, N., & Hickman, S. (in press).

Davatzes, N., & Hickman, S. (2006). Stress And Faulting in the Coso Geothermal Field: Update and Recent Results from the East Flank and Coso Wash. *Thirty-First Workshop on Geothermal Reservoir Engineering.* Stanford.

Haimson, B. C., & Herrick, C. G. (1989). Borehole breakouts and in situ stress. *12th Annual Energy-Sources Technology Conference and Exhibition.* Houston, TX.

Haimson, B., & Fairhurst, C. (1967 йил September). Initiation and extension of hydraulic fractures in rocks. *Soc Pet Eng J* , 310–8.

Jaeger, J. C., & Cook, N. G. (1979). *Fundamentals of Rock mechanics* (2 ed.). New York: Chapman and Hall.

Jaeger, J. C., Cook, N. G., & Zimmerman, R. W. (2007). *Fundamentals Of Rock Mechanics.* Blackwell Publishers.

Kirsch, G. (1898). Die Theorie der Elastizitat und die Bedurfnisse der Festigkeitslehre. VDI Z ;42:707. *Zeitschrift des Vereines deutscher Ingenieure , 42*, 797–807.

Kulander, B., Dean, S., & Ward, B. J. (1990). Fractured Core Analysis: Interpretation, Logging, and Use of Natural and Induced Fractures in Core. *AAPG Methods In Exploration Series* (8), 88.

Li, Y., & Schmitt, D. R. (1997). Well-Bore Bottom Stress Concentration and Induced Core Fractrures. *AAPG Bulletin , 81* (11), 1909-1925.

Lockner, D., & and Beeler, N. (2003). Stress-induced anisotropic poroelasticity response in sandstone. *Electronic Proc. 16th ASCE Engin. Mech. Conf.* U. Washington, Seattle, WA.

Lockner, D., & Beeler, N. (2002). Chapter 32: Rock Failure and Earthquakes. In *International Handbook of Earthquake and Engineering Seismology* (Vol. 81A, pp. 505-537.).

Maerten, F., Maerten, L., Pollard, D., & Lagalay, Y. (2009). Poly3D, a Three-Dimentional Boundary element Method using Angular Dislocations for Sub-Surface structrues Modeling. *J. Geoph. Res.*

Morrow, C. A., & Lockner, D. (2006). *Physical properties of two core samples from well 34-9RD2 at the Coso Geothermal Field, California.*

Peska, P., & Zoback, M. D. (1995). Compressive and tensile failure of inclined well bores and determination of in situ stress and rock strength. *J. Geophys. Res* (100), 12791-12811.

Rose, P., Hickman, S., McCulloch, J., Davatzes, N., Moore, J. M., Kovac, K., et al. (2006). *Creation of an Enhanced Geothermal System through Hydraulic and Thermal Stimulation.*

Sanford, R. J. (2003). *Principles of Fracture Mechanics.* Upper Saddle River, NJ: Prentice Hall.

Soliva, R., Maerten, F., Petit, J.-P., & Auzias, V. (submitted). Fault static friction and fracture orientation in extensional relays; insight from field data, photoelasticity and 3D numerical modeling. *Journal of Structural Geology* .

Tester, J. W., Anderson, B. B., Blackwell, D., DiPippo, R., Drake, E., Garnish, J., et al. (2006). *The Future of Geothermal Energy - Impact of Enhanced Geothermal Systems (EGS) on the United States in the 21st Century.* Masachussets Institute of Technology, Cambridge Masachussets.

The Stanford Rock Fracture Project. (2002). Retrieved 2009 йил August from Stanford University: http://pangea.stanford.edu/research/geomech/Software

Thomas, A. L. (1993). *Poly3D: A Three-Dimensional, Polygonal Element, Displacement Discontinuity Boundary element computer Program with Applications to Fractures, Faults, and Cavities in the Earth's Crust.* Stanford, California.

Townend, J., & Zoback, M. (2000). How faulting keeps the crust strong. *Geology , 28* (5), 399-402.

Zoback, M. D. (2007). *Reservoir Geomechanics.* Cambridge.

Zoback, M. D., Barton, C. A., Brudy, M., Castillo, D. A., Finkbeiner, T., Grollimund, B. R., et al. (2003). Determination of stress orientation and magnitude in deep wells. *International Journal of Rock Mechanics and Mining Sciences , 40* (7-8), 1049-1076.

Zoback, M. D., Mastin, L., & Barton, C. (1987). In situ stress measurements in deep boreholes using hydraulic fracturing, wellbore breakouts and Stonely wave polarization. *Rock stress and rock stress measurements.* Stockholm, Sweden: Centrek Publications, Lulea.

Zoback, M. D., Moos, D., Mastin, L., & Anderson, R. (1985). Well bore breakouts and in situ stress. *Journal of Geophysical Research , 90*, 5523–5530.

Zoback, M., Barton, C., Brudy, M., Castillo, D., Finkbeiner, T., Grollimund, B., et al. (2003). Determination of stress orientation and magnitude in deep wells. *International Journal of Rock Mechanics and Mining Sciences , 40* (7-8), 1049-1076.

APPENDIX

5.1 Appendix A: Well 58A-10 Stress state and section of the mud log

An extensive study to constrain the stress state in the East Flank of the Coso Wash Geothermal Field in California has been performed by Davatzes and Hickman (2006; 2007). The stress state in 58A-10 is best constrained at a true vertical depth below ground level of 2326.5 m. At this depth the vertical principal stress was estimated to be -58.6 MPa assuming an average overburden density of 2.57 g/cc and the formation pore pressure equal to 19.2 MPa by integrating the density of water taking into account its equation of state and the temperature profile in the surrounding formation. The complete Coso stress model is shown in Figure A 1. The section of the mud log relevant to this work is shown in Figure A 2. Note that at a Measure Depth below Ground Level of 2331.1 m (7648 ft) the *WOB* = 25000 lb.

Table 1: Coso stress model (Optimal conditions for Breakout (BO) formation between drilling and image logging)

Data Source	Deviation Log				TPS log		Sonic Log	Strength model	Image log	Density log		Mini-hydrofrac	Calc. from BO analysis
Well	Measured Depth (MD) below GL	Deviation Direction	Deviation From vertical	True Vertical Depth below GL (TVD)	Mud Pressure (P_m)	Formation Fluid Pressure (P_f)	P-wave Velocity (V_P)	Uniaxial Compressive Strength (C_0)	S_{hmin} Azimuth at depth of obs.	Breakout Width (wBO)	Vertical Principal Stress (S_V)	Minimum Horizontal Principal Stress (S_{hmin})	Maximum Principal Horizontal Stress (S_{Hmax})
	[m]	[azi.]	[deg]	[m]	[MPa]	[MPa]	[km/sec]	[MPa]	[azi.]	[deg]	[MPa]	[MPa]	[MPa]
38C-9	1,131.4	340	6.2	1,128.7	11.4 [a]	4.1 [b]	4.94 ±0.60 [d]	188.82 ±27.40 [e]	101	0	29.1 [g]	18.2±0.5 [i]	<85.4 (+11.7,-7.0) [k,l,m]
34-9RD2	2,408.8	311	13	2,382.6	23.5 [a]	7.6 [b]	5.16	192.16 ±18.67 [e]	100	0	61.4 [g]	38.9±1.4 [i]	<117.0 (+6.6 -6.5) [k,m]
58A-10	2,331.1	331	4.2	2,326.5	19.2 [a]	19.2 [c]	5.99 ±0.17 [D]	204.90 ±22.26 [e]	094	33.0 ±9.7 [f]	58.6 [h]	37.9 [j]	100.5 (+8.1, -7.9) [k,m]

Parameters common to all analyses:

$\alpha = 1$ (fluid pressure coefficient in the effective stress law for compressive failure)

$\mu_i = 0.95$ (coefficient of internal friction) which is an equally weighted average of the averaged upper and lower bounds from the USGS measurements (1.29+0.94)/2 on diorite from well 34-9RD2 (Figure 5b) and the TerraTek measurement (0.787) on diorite from well 64-16 (Figure 12a).

Parameters without error bars represent single valued measurements without known formal errors including Measured Depth, Deviation, Deviation Direction, P_m, P_f, V_P and the S_V.

Footnotes:

[a] P_m is minimum pressure in wells prior to logging (*i.e.*, most conducive to breakout formation) as determined from known mud weights and standing mud level in borehole.

[b] For purpose of breakout analysis, P_f is current formation fluid pressure inferred from static TPS logs conducted over intervals of interest when in hydraulic communication with the borehole (*i.e.*, completed open-hole) following long periods of borehole shut-in.

[c] Estimated assuming thermal and hydrostatic equilibrium between P_m and P_f in the near-wellbore environment measured by static TPS logs obtained after long periods of shut in prior to image logging with water table at 274.32 m TVD in well and mud gradient 9.39 kPa/m. This is the minimum $\Delta P = P_m - P_f$ prior to logging and the most favorable condition for breakout formation.

[d] Since V_P logs are not available in 38C9, the average and one standard deviation of V_P measured in the upper 150 m, from 1450 to 1600 m MD below GL, of 34-9RD2 less than 1 km away is used.

[D] One standard deviation error estimate over interval from 2310.38 to 2331.72 MD below GL in which 57 BO occur in tight clusters at local minima in V_P.

[e] Errors in C_0 are the addition of one standard deviation in the V_P log over the depth of interest and one standard deviation due to scatter in the correlation of V_P to C_0 in the strength model which is estimated in Figure 12b.

[f] Breakouts analysis was performed nearest the depth of the mini-hydraulic fracturing measurement of S_{hmin} in well 34-9RD2 at 2313.43 to 2391.16 m MD below GL and with an average depth of 2331.14 m MD below GL or 2326.66 m TVD (see boxed interval in Figure 13a). Analyzing wBO within this narrow depth interval quantifies the sensitivity of the analysis to wBO variation.

[g] Estimated from the depth weighted average rock density of 2.65 g/cc from surface to depth obtained from a geophysical density log in well 34-9RD2 from 1102.00 to 1980.29 m MD. This average rock density is consistent with lab measurements of diorite (Figure 3) and provides a reasonable representation of rock density in the geothermal field as it samples a large depth interval within the reservoir.

[h] Well 58A-10 passes through 552.60 m of sediment with estimated density of 2.3 g/cc and through 2,108.30 m of crystalline rock with estimated density of 2.65 g/cc [g].

[i] Error represents the range of ISIP observed during repeated pressure cycling in the mini-hydraulic fracturing experiments of 38C-9 (Sheridan and Hickman, 2004) and 34-9RD2 (Davatzes and Hickman, 2006) respectively.

[j] Estimated from the East Flank S_{hmin} gradient defined by the mini-hydraulic fracturing measurements in wells 38C-9 and 34-9RD2. Sensitivity of the calculated S_{Hmax} to the estimate of S_{hmin} is analyzed in Figure 13c. S_{hmin} azimuth is from Sheridan and Hickman (2004) and Davatzes and Hickman (2006).

[k] Reported uncertainty in S_{Hmax} from uncertainties shown in C_0 and wBO are propagated through the analysis by making the conservative assumption that they are uncorrelated and thus additive. For 38C-9 and 34-9RD2 uncertainty is also derived from S_{hmin}.

[l] Upper bound on S_{Hmax} is less reliable because no V_P log was available to constrain C_0.

[m] The effects of thermal stresses due to cooling of the well are neglected in the analysis of breakouts.

Figure A 1. Stress state table reproduced from Davatzes and Hickman (2006; 2007)

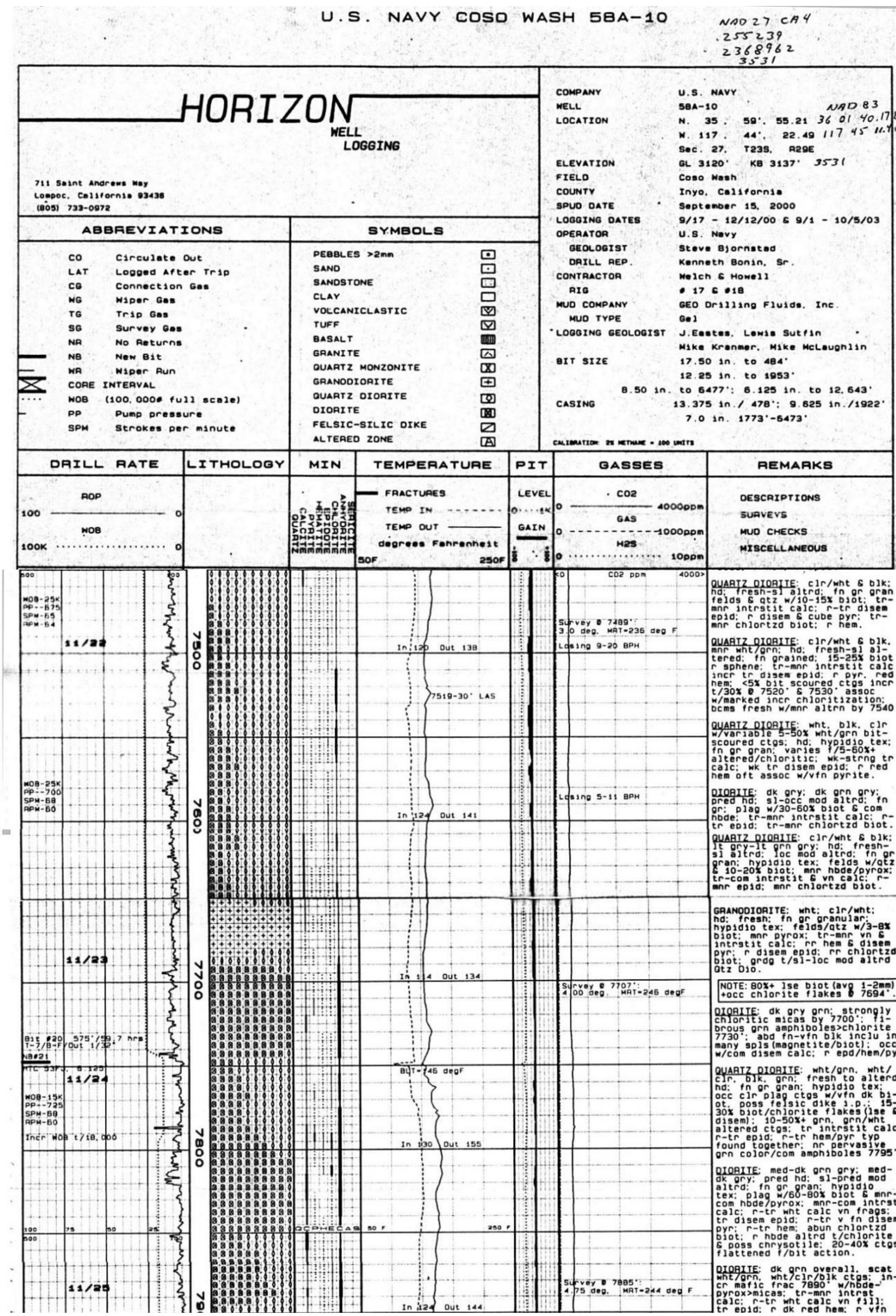

Figure A 2. Mud Log of Well 58A-10 in the Coso Geothermal Field, California.

5.2 Appendix B: Additional visualization comparing analytical and Poly3D solutions

In order to better elucidate how closely the stress concentration numerically computed with Poly3D for the selected case (40 circumferential elements) followed the Kirsch analytical solution, the principal local stresses σ_1 and σ_3 as well as the stress components σ_{xx}, σ_{yy} and σ_{xy} were plotted as a white dotted line on top of the Kirsch solution in Figure B 1**Error! Reference source not found.**. **Error! Reference source not found.** Figure B 2 shows the percent error plot between both solutions; note that as the stress survey gets farther away from the well surface the percent error drops dramatically and matches the Kirsch solution. The contour bar scale shows the percent error from 20 to -20%. This set of plots with the low overall percent error support the decision of picking a well mesh with 40 circumferential elements as the minimum optimum density mesh.

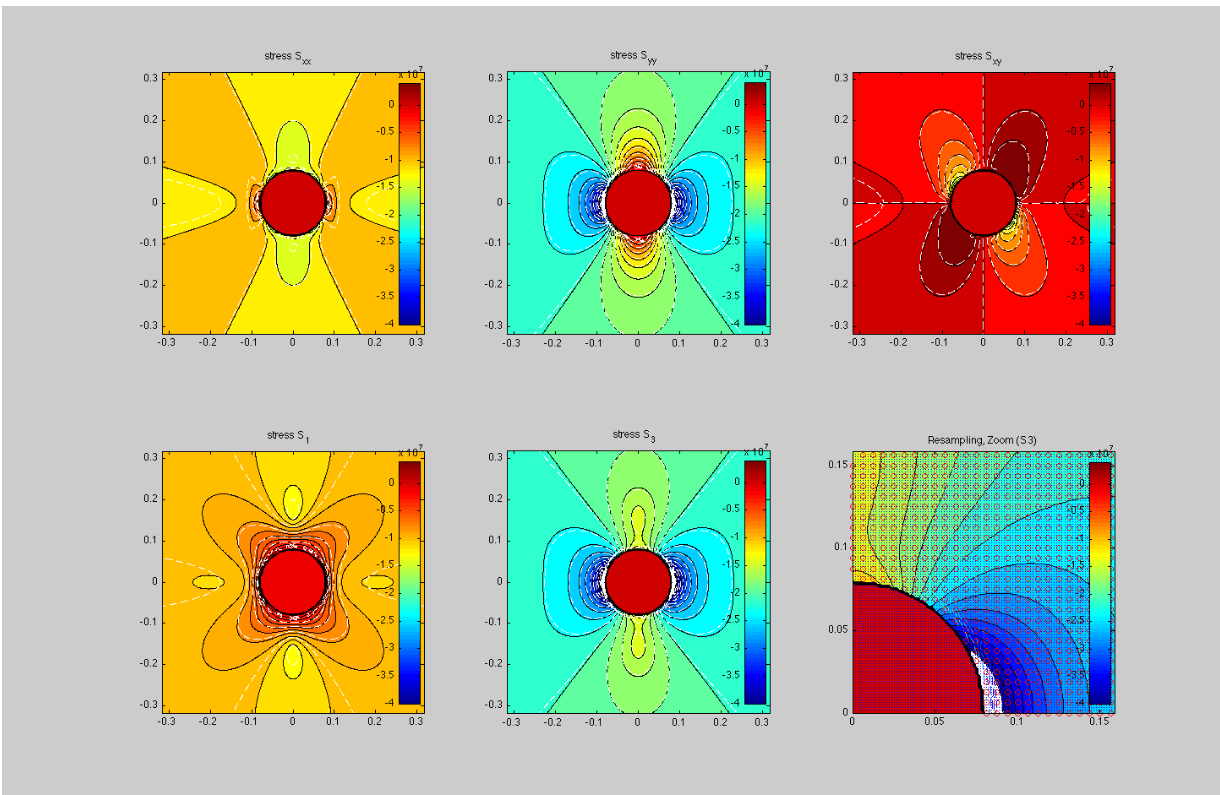

Figure B 1. Concentration of stresses in a model with 40 circumferential elements (white dotted line) compared with the corresponding analytical Kirsch solution shown with solid lines and color contour. Note that in the bottom right figure, the dots represent the locations of observation points used in both the analytical and numerical calculations used to contour stress components.

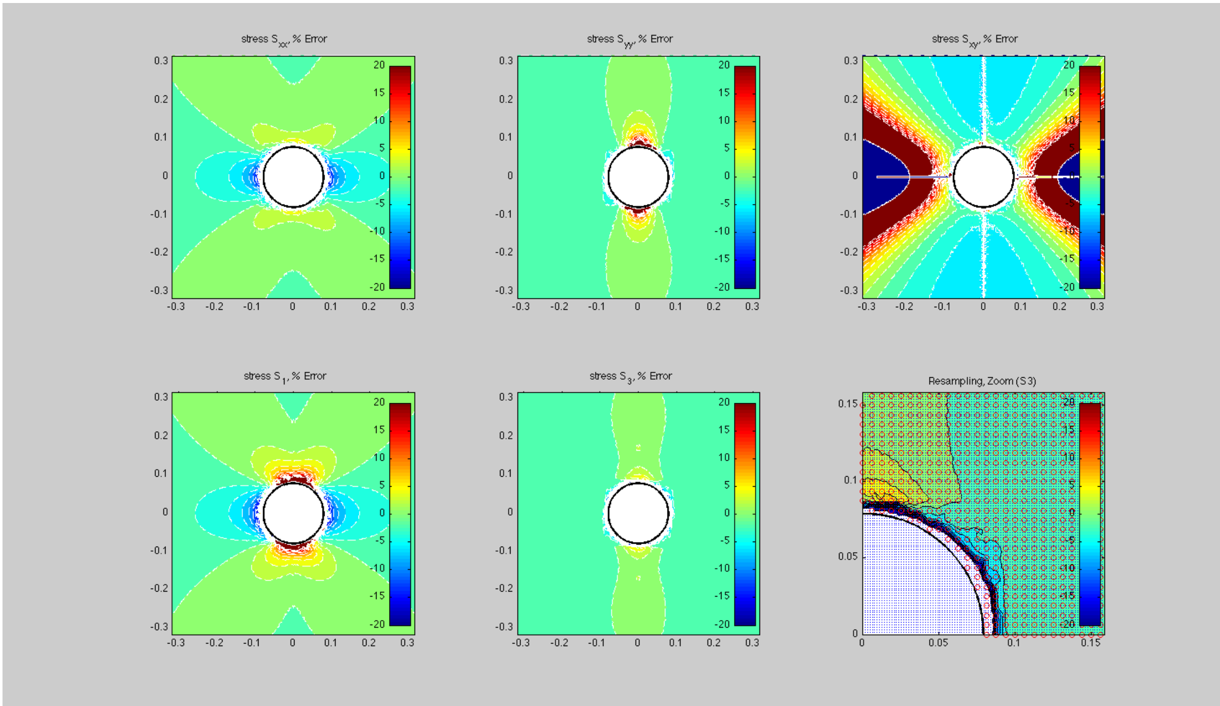

Figure B 2. Errors plot of the model concentration of stresses against the Kirsch solution. Circles in bottom right reveal location of observation points used to construct contours.

5.3 Appendix C: Kirsch Solution for well 58A-10

Figure C 1a) shows the stress variation on the wall, where r=R (Equations(1) and (2)), of the $\sigma_{\theta\theta}$ and σ_{rr} components. Because the borehole wall is a traction free surface, these stress components are principal stresses. The σ_{rr} component is -2.48 MPa equivalent to the compression induced from *dP* regardless of direction, θ. $\sigma_{\theta\theta}$ varies relative to the angle with the remote horizontal principal stresses. It is in tension over a portion of the borehole wall ±20° from the direction of S_{Hmax}. In contrast, compression in $\sigma_{\theta\theta}$ is maximized in the direction of S_{hmin} direction and exceeds the -204.9 MPa uniaxial compressive strength measured in rock mechanics experiments of rock in the reservoir (Morrow & Lockner, 2006) ±17° from S_{hmin}. Both results are consistent with the occurrence of tensile fractures and breakouts respectively visible in image log of borehole 58A-10 (Rose, et al., 2006). The variation in the concentration of stress components σ_{rr}, $\sigma_{r\theta}$ and $\sigma_{\theta\theta}$ along the direction of application of S_{Hmax} (θ = 0°) in which tension is maximized as the distance from the well increases is show in **Error! Reference source not found.**b). The S_{rr} component starts at a stress magnitude of -.48 MPa due to the mud pressure in excess of formation fluid pressure and slowly converges to that of the effective principal stress in that direction, $\sigma'_{Hmax} = (S_{Hmax} - P_p) = -81.3$ MPa. The $\sigma_{r\theta}$ component is zero in the whole θ = 0 direction due to the shear traction free surface of the well. The $\sigma_{\theta\theta}$ stress component starts at a tensile stress magnitude of 27.5 MPa and quickly drops to that of the effective principal stress in that direction, $\sigma_{hmin} = (S_{hmin} - P_p) = -18.7$ MPa as it advances away from the well. Consequently, **Error! Reference source not found.**c) hows the variation in the concentration of stress components σ_{rr}, $\sigma_{r\theta}$ and $\sigma_{\theta\theta}$ along the direction of application of S_{hmin} (θ = 90°) in which compression is maximized as the distance from the well increases. The σ_{rr} component starts at a stress magnitude of -2.48 MPa and converges to that of the effective principal stress in that direction, $\sigma'_{hmin} = (S_{hmin} - P_p) = -18.7$ MPa. The $\sigma_{r\theta}$ component is again zero in the whole $\theta = 0$ direction due to the shear traction free surface of the well. The $\sigma_{\theta\theta}$ component starts at a compressive stress magnitude of -223 MPa which corresponds to the maximum amplification of compressive stress on the wall and converges to that of the effective principal stress in that direction, $\sigma'_{Hmax} = (S_{Hmax} - P_p) = -81.3$ MPa as the distance from the well is increased.

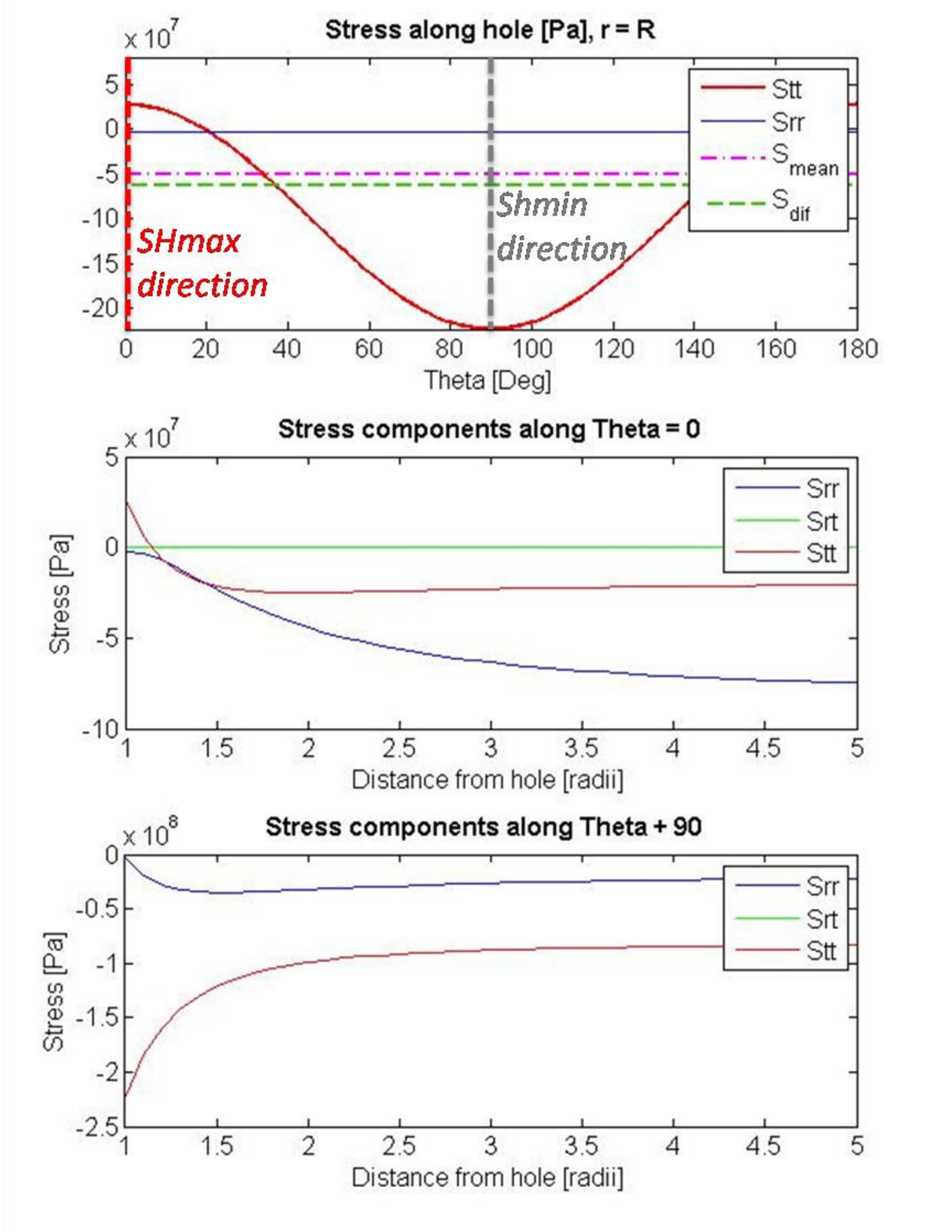

Figure C 1. Stress variation simulated using the Kirsch solution for 2D plane strain along the wall of a borehole using the stress state in well 58A-10 at 2326.5 m true vertical depth below ground level. (a) Variation in the stress components along the well surface from 0° to 180°. Variation in the stress components along (b) the S_{Hmax} principal direction at 0° and (c) the S_{hmin} principal stress direction at 90°.